



**HAL**  
open science

# Porosity and permeability evolution in the Tuaheni Landslide Complex at Hikurangi margin from IODP Sites U1517 and U1519

Jade Dutilleul, Sylvain Bourlange, Yves Géraud, Thierry Reuschlé

► **To cite this version:**

Jade Dutilleul, Sylvain Bourlange, Yves Géraud, Thierry Reuschlé. Porosity and permeability evolution in the Tuaheni Landslide Complex at Hikurangi margin from IODP Sites U1517 and U1519. *New Zealand Journal of Geology and Geophysics*, 2021, pp.1-19. 10.1080/00288306.2021.1990088 . hal-03419744v2

**HAL Id: hal-03419744**

**<https://hal.science/hal-03419744v2>**

Submitted on 14 Feb 2022

**HAL** is a multi-disciplinary open access archive for the deposit and dissemination of scientific research documents, whether they are published or not. The documents may come from teaching and research institutions in France or abroad, or from public or private research centers.

L'archive ouverte pluridisciplinaire **HAL**, est destinée au dépôt et à la diffusion de documents scientifiques de niveau recherche, publiés ou non, émanant des établissements d'enseignement et de recherche français ou étrangers, des laboratoires publics ou privés.



Distributed under a Creative Commons Attribution - NonCommercial - NoDerivatives 4.0 International License

1 **Porosity and permeability evolution in the Tuaheni Landslide Complex**  
2 **at Hikurangi margin from IODP Sites U1517 and U1519**

3 Jade Dutilleul<sup>a\*</sup>, S. Bourlange<sup>b</sup>, Y. Géraud<sup>b</sup> and T. Reuschlé<sup>c</sup>

4 *<sup>a</sup>University of Lorraine, CNRS, GeoRessources, F-54000 Nancy, France, now at*  
5 *Earthquake Research Institute, The University of Tokyo, Tokyo, Japan*

6 *<sup>b</sup>University of Lorraine, CNRS, GeoRessources, F-54000 Nancy, France*

7 *<sup>c</sup>Université de Strasbourg, CNRS, Institut Terre et Environnement de Strasbourg, UMR*  
8 *7063, 5 rue Descartes, Strasbourg F-67084, France*

9 [\\*jade.dutilleul@univ-lorraine.fr](mailto:jade.dutilleul@univ-lorraine.fr); [jdutilleul@eri.u-tokyo.ac.jp](mailto:jdutilleul@eri.u-tokyo.ac.jp)

10

11 Several mechanisms involving excess pore pressure related to gas hydrate have  
12 been proposed to explain active creeping at landslides such as the north  
13 Hikurangi margin Tuaheni Landslide Complex (TLC). Cores and logging data  
14 were retrieved by the International Ocean Discovery Program (IODP)  
15 Expeditions 372 and 375 from the South TLC at Site U1517. Here, the evolutions  
16 of porosity, pore structure and permeability are determined to assess the  
17 compaction state in the landslide and compare it with that of the undeformed  
18 sequence at Site U1519. Although no evidence of gas hydrate in the landslide at  
19 Site U1517 was identified by the cruise, zones suspected to host gas hydrates  
20 below the landslide or at Site U1519 are characterised by higher porosity, pore  
21 diameter and permeability. We show that most of the sedimentary section is in  
22 hydrostatic conditions, except the base of the TLC at Site U1517 and a zone  
23 below the base of the gas hydrate stability zone at Site U1519. These zones might  
24 be candidates for excess pore pressure build-up. There is no obvious evidence of  
25 the involvement of gas hydrate in active creeping at the TLC, which is more  
26 likely induced by hydrogeomechanical processes.

27 Keywords: porosity, permeability, pore pressure, gas hydrates, MICP, NMR,  
28 CEC, landslide, Hikurangi, IODP

29 **Introduction**

30           The Tuaheni Landslide Complex (TLC) is situated on the upper slope of the  
31 relatively sediment-starved north Hikurangi margin (Mountjoy et al., 2009), where the  
32 Pacific Plate obliquely subducts, at a ~5.0 cm/y rate, beneath the Australian Plate  
33 (Wallace et al., 2004) (Figure 1a). In the study area, the Pacific Plate is composed of the  
34 Cretaceous-aged volcanic Hikurangi Plateau protruded by seamounts and blanketed by a  
35 ~1.0–1.5 kilometres-thick Cenozoic to Mesozoic sedimentary cover. The TLC is  
36 composed of Quaternary shelf-edge clinoform sequences (Pedley et al., 2010), with  
37 wedge-shaped thinning-upwards siliciclastic sediments (Barnes et al., 1991; Alexander  
38 et al., 2010), above Cenozoic and Late Mesozoic sediments (Field et al., 1997; Barnes et  
39 al., 2002; Mountjoy and Barnes, 2011). Based on morphological differences, Mountjoy  
40 et al. (2009) divided the TLC into a north (North TLC) and a south component (South  
41 TLC) (Figure 1b), both feeding the Tuaheni Basin with Quaternary sediments  
42 (Mountjoy et al., 2009; 2014). The South TLC also contributes to filling the Paritu  
43 Basin with debris. Arcuate internal scarps characterise the North TLC. The South TLC,  
44 on which this study is focused, is constituted by irregular rough landslide debris  
45 downslope of large scarps. The South TLC is thought to be divided into two mass-  
46 transport deposit (MTD) units (Mountjoy et al., 2014; Böttner et al., 2018; Gross et al.,  
47 2018; Kuhlmann et al., 2019). These units are separated by an intra-debris negative-  
48 polarity seismic reflector, interpreted as a décollement layer that may localise excess  
49 pore pressure (Gross et al., 2018).

50           Based on bathymetry data, Mountjoy et al. (2009) suggested that the South TLC  
51 initially formed as a catastrophic failure and is now actively creeping, rather than  
52 growing through repeated failures leading to downslope transport of new source  
53 material, as commonly admitted for submarine landslides (Mulder and Cochonat, 1996;

54 Canals et al., 2004). However, the mechanisms triggering this active slow deformation  
55 remain unclear. First, Mountjoy et al. (2009) related creeping with high pore pressure  
56 induced by gas expulsion, sediment loading or earthquakes. Such creeping would  
57 conduct to small-scale compressional and extensional features across the landslide,  
58 which have not been observed. On the contrary, the South TLC is marked by a  
59 transition from a compressive upper sediment-supplied mass to an extensive part near  
60 the toe where sediments are removed (Figure 2a) (Mountjoy et al., 2014; Barnes et al.,  
61 2019a). Later, Mountjoy et al. (2013, 2014) observed that the upper limit of creeping  
62 occurs downslope of where a hydrate-related bottom-simulating-reflector (BSR) (and  
63 thus the base of gas hydrate stability (BGHS)) cutting through the landslide reaches the  
64 seafloor. This zone also corresponds to the transition between compressional and  
65 extensional deformation of the South TLC. They suggested that gas hydrates may be  
66 involved in ongoing slow deformation and proposed three possible mechanisms: 1) gas  
67 hydrate dissociation at the BGHS; 2) a hydrate pressure valve model implying the  
68 repeated hydrofracturing and weakening of the gas hydrate zone with a transfer of the  
69 overpressure accumulated underneath low-permeability gas hydrate-bearing sediments  
70 to the landslide mass where the BGHS approaches the seafloor and 3) a hydrate glacier  
71 model with gas hydrate-bearing sediments showing creeping behaviour (Mountjoy et  
72 al., 2013, 2014; Barnes et al., 2019a).

73         The International Ocean Discovery Program (IODP) Expedition 372 drilled,  
74 logged and cored Site U1517 in the extensional zone of the south component (Figures  
75 1b and 2) to investigate the mechanisms behind creeping in the TLC and their possible  
76 links with gas hydrate occurrence. Gas hydrates were identified beneath the landslide  
77 based on drilling results, discarding the hydrate glacier model hypothesis (Barnes et al.,  
78 2019c; Sreaton et al., 2019). Two other sites were initially planned to be drilled in the

79 compressive part of the landslide and a reference site outside the landslide mass (Pecher  
80 et al., 2014). Even if this second drilling phase was not achieved (Barnes et al., 2019a),  
81 the outcomes from Site U1517 (Barnes et al., 2019b) can be interpreted in light of the  
82 properties of the sedimentary section at Site U1519 (Barnes et al., 2019a). Site U1519  
83 was drilled, logged and partially cored ~15 kilometres at the northeast of Site U1517, in  
84 the western part of the Tuaheni basin fed by the north component of the TLC (Figures  
85 1b and 3) (Barnes et al., 2019c). Gas hydrate occurrence is inferred from direct  
86 observations at Site U1519 (Barnes et al., 2019c).

87         Here, we document the evolution of compaction state from porosity and  
88 permeability from measurements on core samples and logging-while-drilling (LWD)  
89 data at Site U1517 through the extensional part of the South TLC and beneath, and at  
90 Site U1519. Compaction state may be interpreted in terms of pore pressure  
91 development. Elevated pore pressure is commonly associated with a local anomalously  
92 high porosity compared to a reference porosity-effective stress curve (Conin et al.,  
93 2011) determined assuming hydrostatic fluid pressure and uniaxial compaction  
94 conditions (Screaton et al., 2002). However, the porosity routinely measured on core  
95 samples during IODP expeditions cannot be directly used for compaction state analysis  
96 because it is based on the total water content of samples. Total water content includes  
97 interstitial water, which is contained in pores, and water bound in hydrous minerals such  
98 as smectite (Brown and Ransom, 1996; Henry, 1997). Smectite-bound water is mainly  
99 released in the pore space by dehydration to illite, which is generally assumed to occur  
100 in a temperature range of 60–150°C (Freed and Peacor, 1989; Kastner et al., 2014). In  
101 contrast, interstitial water is expelled from the pore structure by pore collapse induced  
102 by compaction as sediments are buried (Moore and Vrolijk, 1992). Thus, interstitial  
103 water is truly representative of the compaction state (Henry, 1997; Henry and

104 Bourlange, 2004; Conin et al., 2011). Hence, we quantify interstitial porosity by  
105 correcting total porosity measured on samples from the smectite-bound water content to  
106 determine the compaction state at both sites. We also compare permeability deduced  
107 from pore size distribution with the permeability measured on two samples (cores 17H6  
108 and 29F3 at 97.43 and 157.83 mbsf respectively) in a triaxial cell under effective  
109 hydrostatic confining pressure approaching in-situ stress conditions. Finally, we discuss  
110 the porosity and permeability dataset in terms of pore pressure development at both  
111 Sites U1517 and U1519. We address the hypotheses (i.e. gas hydrates are involved in  
112 creeping in the TLC either through gas hydrate dissociation at the BGHS or hydrate  
113 pressure valve effect) and antitheses (i.e. creeping is induced by other mechanisms such  
114 as repeated small-scale seafloor failure or liquefaction of coarse silt beds) suggested  
115 during IODP Expedition 372 (see Barnes et al., 2019a for details) as possible  
116 mechanisms triggering slow deformation in the TLC.

## 117 **Material and data**

### 118 *Site U1517*

119 Site U1517 provided core samples and in-situ geophysical data including LWD  
120 data, and temperature and pressure measurements down to ~205 mbsf (Figure 4a). Five  
121 lithological, seismic and logging units were identified onboard (Barnes et al., 2019b).  
122 Lithological Unit I (~0–3 mbsf) corresponds to Holocene-aged greenish-grey silty clay.  
123 Units II, III and IV are Late Pleistocene-aged. Unit II (~3–41 mbsf) is composed of a  
124 succession of stacked turbidites with alternating layers of mud (i.e. clayey silt to silty  
125 clay) and greenish-grey sand beds. Unit III (~41–67 mbsf) corresponds to matrix-  
126 supported MTDs with thin to medium bedded convoluted mud layers and alternating  
127 layers of greenish-grey silt and clay. Unit IV (~67–103 mbsf) is a greenish-grey to dark

128 greenish grey massive clayey silty hemipelagic sequence with MTDs at the top and  
129 punctuated with silty turbidites at the base. Unit V (~103–187 mbsf) is a Middle  
130 Pleistocene mixed slope sequence including clayey to clayey–silt hemipelagites, sandy  
131 turbidites, MTDs and ash layers near the bottom of the hole.

132 Above the upper part of the preslide interval (~67–203 mbsf), the South TLC  
133 mass was interpreted to be composed of Unit II (upper debris unit) and Unit III (lower  
134 debris unit) (Mountjoy et al., 2014; Gross et al., 2018; Barnes et al., 2019b; Luo et al.,  
135 2020), with the décollement for creeping ~37 mbsf corresponding to the intra-debris  
136 negative polarity reflector of Gross et al. (2018). Mountjoy et al. (2014) suggested that  
137 the upper and lower units were genetically linked. This model has been recently  
138 challenged by studies that highlight different source and/or emplacement mechanisms.  
139 Luo et al. (2020) suggest that the landslide was formed by two different depositional  
140 events corresponding to Units II and III, while Couvin et al. (2020) propose that the  
141 landslide is only composed of the upper Unit II.

142 The base of the gas hydrate stability zone (BGHS) has been interpreted to occur  
143 ~162 mbsf prior to drilling (Gross et al., 2018; Barnes et al., 2019b; Sreaton et al.,  
144 2019, 2020) or between ~85 and 128 mbsf (Sultan, 2020). Indication for gas hydrate  
145 occurrence was only found in Unit V (Figure 4) (Barnes et al., 2019b; Sreaton et al.,  
146 2019, 2020; Sultan, 2020).

#### 147 ***Site U1519***

148 Site U1519 was drilled and logged down to 650 mbsf across three seismic units:  
149 1) horizontally layered basin–fill including stacked MTDs and turbiditic sequences (~0–  
150 281 mbsf), the upper MTD being associated with the North TLC (Mountjoy et al., 2009,  
151 2014; Barnes et al., 2019c), 2) southeast–dipping layered slope sequences of MTDs  
152 truncated at the unconformity between seismic Units 1 and 2 (~281–546 mbsf) and the

153 top (~546–650 mbsf) of a northwest-dipping and eroded hanging-wall of an inactive  
154 northwest-dipping splay fault that lies ~500 metres beneath the bottom of Site U1519  
155 (Figure 3). Site U1519 crosscuts a weak reflector at ~560 mbsf interpreted as a possible  
156 BSR. Several intervals were cored: ~0–23 mbsf at hole D, ~0–86 mbsf at hole E and  
157 ~10–164 mbsf, ~250–288 mbsf and ~518–640 mbsf at hole C. Based on core  
158 examination, two lithological units were identified during the cruise (Barnes et al.,  
159 2019c) (Figure 5). Unit I corresponds to Holocene to late middle Pleistocene dark  
160 greenish grey mud to mudstone (i.e. silty clay(stone) to clayey silt(stone)) associated  
161 with hemipelagic settling with an ash layer occurring few meters below the seafloor.  
162 Unit I is correlated with seismic Unit 1 and logging Unit 1. Seismic and logging Units 2  
163 and 3 correspond to lithologic Unit II, including middle to early Pleistocene light  
164 greenish-grey mudstone with scattered interbeds of silt and very fine sand, medium to  
165 coarse sand, and contorted mudstone interpreted as MTDs. Gas hydrate-bearing  
166 sediments were sampled in the lower part of the hole in core 25R4 (~627 mbsf, Figure  
167 5) (Barnes et al., 2019c).

## 168 **Methods**

169 This study is based on 1) onboard data including LWD data and measurements  
170 on core samples and 2) post-cruise analysis of 24 and 40 core samples retrieved at Site  
171 U1517 and U1519, respectively. Samples were selected near the samples that were used  
172 for pore water composition analysis onboard. Samples were conditioned for shipping  
173 and stored at chilled temperature (2–8°C) in vacuum-sealed plastic bags with a sponge  
174 saturated with seawater to retain moisture.



175 **Porosity**

176 *Total connected porosity*

177 We calculated the total connected porosity ( $\phi_t$ ) with a Micromeritics® AccuPyc  
178 II 1340 helium-displacement pycnometer using the procedure after Blum (1997) that  
179 was also followed onboard (Wallace et al., 2019; Pecher et al., 2019).

180 *Bound water content*

181 Clay bound water includes 1) water molecules absorbed in the interlayer space  
182 that are usually organised into layers and 2) water molecules adsorbed on smectite  
183 external surfaces and are electrostatically bounded to hydrated cations compensating the  
184 negative charge of smectite layers. Clay-bound water content ( $\phi_b$ ) was calculated using  
185 Equation (1):

186 
$$\phi_b = n \frac{M_w}{\rho_w} CEC \rho_g (1 - \phi_t) \quad (1)$$

187 based on the cation exchange capacity (CEC, in mol/kg) that is a proxy for hydrous to  
188 non-hydrous minerals content ratio, the water molar mass ( $M_w = 0.018\text{kg/mol}$ ) and  
189 density ( $\rho_w = 1024 \text{ kg/m}^3$ ), the grain density ( $\rho_g$  in  $\text{kg/m}^3$ ) and  $n$  the average number of  
190 water molecules per cation charge related to the number of water layers in the clay  
191 interlayer space. The average number of water molecules per cation charge is typically  
192 determined from the relationship between the CEC and the volume of chloride-free  
193 water per volume of grains (Figure 6) that is derived from the soluble chloride content  
194 of the sample (Henry and Bourlange, 2004; Conin et al., 2011; Daigle et al., 2015a;  
195 Dutilleul et al., 2020a; 2020b). The average number of water molecules per cation  
196 charge commonly ranges 6–8, 12–16, and 18–24 for one, two or three water layers  
197 respectively (Henry, 1997). All the samples at Sites U1517 and U1519 show low CEC  
198 values  $<0.2 \text{ mol/kg}$  and thus do not show a specific bound water ratio versus CEC trend

199 from which  $n$  can be inferred (see Henry and Bourlange, 2004; Dutilleul et al., 2020a  
200 for further details). We used the average value of  $n=15$  which is typical of smectite with  
201 two water layers occurring in marine sediments (Kastner et al., 2014), following the  
202 results of Dutilleul et al. (2020b).

### 203 *Interstitial porosity and compaction trends*

204 Interstitial porosity ( $\phi_i$ ) was obtained by correcting the total connected porosity ( $\phi_t$ ) for the clay-bound water content ( $\phi_b$ ) following Equation (2):

$$206 \quad \phi_i = \phi_t - \phi_b \quad (2)$$

207 The ‘onboard interstitial porosity’ was determined by extrapolating bound water  
208 content measured on samples to correct the total connected porosity values that were  
209 measured onboard on 153 samples at Site U1517 and 278 samples at Site U1519. At  
210 Site U1517, where extensive coring was implemented, we used onboard interstitial  
211 porosity data to determine compaction curves (Figure 7). Instead, at Site U1519 where  
212 coring was restricted to limited intervals, we used resistivity-derived porosity calibrated  
213 to onboard interstitial porosity.

### 214 *Resistivity-derived porosity*

215 For clay-rich materials, which characterised by high electrical surface  
216 conductivity, we estimated resistivity-derived porosity from LWD resistivity using the  
217 model by Revil et al. (1998). In this model, the resistivity-derived porosity ( $\phi$ ) is related  
218 to the formation factor  $F$  based on Archie’s law (Archie, 1942) as expressed by  
219 Equation (3) where  $a$  and  $m$  are constants.

$$220 \quad F = a \phi^{-m} \quad (3)$$

221 Conin et al. (2011) and Dutilleul et al. (2020b) have shown that in siliciclastic and  
 222 volcanoclastic clay-rich sediments, resistivity-derived porosity fits interstitial porosity  
 223 using  $a=1$  and adjusting the cementation factor ( $m$ ) between 1 and 3.5.  
 224  $F$  was determined with Equation (4) based on the bulk electrical conductivity ( $\sigma$ ), the  
 225 electrical surface conductivity ( $\sigma_s$ ) and the electrical conductivity of the interstitial fluid  
 226 ( $\sigma_{if}$ ) as:

$$227 \quad F = \frac{\sigma_{if}}{\sigma} \left[ 1 + 2 \frac{\sigma_s}{\sigma_{if}} \left( \frac{\sigma_{if}}{\sigma} - 1 \right) \right] \quad (4)$$

228 since the hypotheses of Bussian (1983) and Bourlange et al. (2003) are valid at Site  
 229 U1517 where  $\frac{\sigma_s}{\sigma_{if}} \ll 1$ .

230 We used ring resistivity which has the highest vertical resolution for the depth  
 231 penetration (Barnes et al., 2019c) to determine  $\sigma$ .

232  $\sigma_{if}$  was determined using Equation (5) from the concentrations of  $\text{Cl}^-$ ,  $\text{Na}^+$ ,  $\text{K}^+$ ,  $\text{Ca}^{2+}$ ,  
 233  $\text{Mg}^{2+}$  and  $\text{SO}_4^{2-}$  in interstitial water ( $C_{iws}^i$ ) and seawater ( $C_{sw}^i$ ), the ionic mobility in the  
 234 fluid ( $\beta_f^i$ ), the number of charges of ions ( $Z_i$ ) and the seawater conductivity ( $\sigma_{sw}$ ).

$$235 \quad \sigma_{if} = \sigma_{sw} \frac{\sum_i (\beta_f^i \times Z_i \times C_{iws}^i)}{\sum_j (\beta_f^j \times Z_j \times C_{sw}^j)} \quad (5)$$

236 The seawater conductivity was calculated using Equation (6) based on temperature  $T$  (in  
 237 °C).

$$238 \quad \sigma_{sw} = 5.32(1 + 0.02(T - 25)) \quad (6)$$

239 At Site U1517,  $T(^{\circ}\text{C}) = 5.32 + 39.8 \times 10^{-3} z$  (7) where  $z$  is the depth (in mbsf) (Barnes et  
 240 al., 2019b) while  $T(^{\circ}\text{C}) = 5.70 + 24.3 \times 10^{-3} z$  (8) at Site U1519 (Barnes et al.,  
 241 2019c).

242 The model developed by Revil et al. (1998) assumes a major contribution of the Stern  
243 layer to surface electrical conduction, spherical grains and a linear temperature  
244 dependency of the exchangeable cation mobility ( $\beta_s$ ) to quantify  $\sigma_s$  with Equation (9):

$$245 \quad \sigma_s = \frac{2}{3} \rho_g CEC \beta_s \quad (9)$$

## 246 ***Pore size distribution***

### 247 *Mercury injection capillary pressure (MICP)*

248 The distribution of the size of pore throats from 360  $\mu\text{m}$  to 5.7 nm was  
249 determined by MICP experiments performed with a Micromeritics® AutoPore IV 9500  
250 at room temperature (20°C). Samples were formerly oven-dried at 105°C $\pm$ 5°C for 24h.  
251 During the low-pressure analysis, the samples were first degassed under vacuum. The  
252 cell was then gradually intruded by a measured volume of mercury up to a mercury  
253 pressure of  $\sim$ 0.2 MPa. Next, we used a high-pressure analysis sequence whereby we  
254 measured the volume of intruded mercury filling the cell and the sample at a known  
255 pressure that was increased stepwise to 220 MPa. This stage provides the distribution of  
256 the size of pore throats using the Young-Laplace Equation (10) (Purcell, 1949):

$$257 \quad r = \frac{2 \sigma_{Hg} \cos \theta_{Hg}}{P_{Hg}} \quad (10)$$

258 from the pore throat radius ( $r$  in m), the air-mercury interfacial tension ( $\sigma_{Hg}$ =0.485  
259 N/m), the mercury-sediment contact angle ( $\theta_{Hg}$ =140°) and the mercury injection  
260 pressure ( $P_{Hg}$  in Pa).

### 261 *Nuclear magnetic resonance (NMR)*

262 A Bruker® Minispec Mq20 was used to perform proton NMR measurements at  
263 room temperature (20°C) and atmospheric pressure on core samples with a diameter of

264 8 mm. Proton NMR records the magnetisation decay of the hydrogen nuclei of water  
 265 molecules in a saturated porous sample when static and pulsed magnetic fields are  
 266 applied. We measured the transverse relaxation time ( $T_2$ ) that provides insight into void  
 267 size and porosity (Daigle et al., 2014; Bossennec et al., 2018) applying the Carr-Purcell-  
 268 Meiboom-Gill (CPMG) sequence (Carr and Purcell, 1954; Meiboom and Gill, 1958).  
 269 We used a recycle delay of 0.1 s, a half-echo time  $\tau$  of 0.04 ms (the minimum  
 270 obtainable for this equipment), gain ranging around 70–80%, 200 echoes per scan and  
 271 128 scans were stacked (Duttilleul et al., 2020b). The raw  $T_2$  exponential decay  
 272 measured was inversed in a smoothed  $T_2$  distribution using UpenWin© software. We  
 273 used the Equation (11) following Marschall et al. (1995) to correlate the  $T_2$  (in s)  
 274 measured by LWD NMR to MICP pore throat radius (here, in  $\mu\text{m}$ ) based on the  
 275 effective relaxivity ( $\rho_e$ , in  $\mu\text{m/s}$ ):

$$r = 2\rho_e T_2 \quad (11)$$

277 We extrapolated the effective relaxivity across coring gaps where no MICP data were  
 278 available to determine an average pore radius profile across Sites U1517 and U1519  
 279 based on LWD NMR data.

280 NMR porosity ( $\phi$ ) (Daigle et al., 2014) was determined using Equation (12) with the  
 281 volume of dry grains ( $V_g$ ) from the helium-displacement pycnometer and the volume of  
 282 water ( $V_w$ ) in the sample.

$$\phi_{NMR} = \frac{V_w}{V_w + V_g} \quad (12)$$

284  $V_w$  was quantified using a calibration (Equation (13)) in which the maximum signal  
 285 amplitude  $A_0$  (corrected for the gain) was recorded during the  $T_2$  measurement for  
 286 known volume of water.

$$V_w = 19.762A_0 - 0.092 \quad (R^2=0.94) \quad (13)$$

288 NMR porosity was also measured onboard using the Schlumberger ProVisionPlus  
289 logging tool.

## 290 ***Permeability***

### 291 *Permeability measurements under confining pressure*

292 Permeability measurements were conducted at room temperature, in a 200 MPa  
293 hydrostatic pressure cell equipped with a pore fluid pressure circuit (Reuschlé, 2011).  
294 Experiments were run on two cylindrical samples (20 mm in diameter and 40 mm in  
295 length) from the preslide interval at Site U1517 at 97.43 mbsf (core 17H6, lithological  
296 Unit IV) and 157.83 mbsf (core 29F3, Unit V) respectively. Permeability was measured  
297 on the initial saturated samples using a pulse decay method (Brace, 1984): an initial  
298 imposed differential pore fluid pressure ( $\Delta P_p$ ) is applied to equilibrate through the  
299 sample. Its decay is approximately exponential and the decay time is inversely  
300 proportional to the permeability following Equations (14) and (15) (Hsieh et al., 1981;  
301 Reuschlé, 2011):

$$302 \quad \Delta P_p(t) \propto \exp(-\alpha t) \quad (14)$$

303 and

$$304 \quad \alpha = [Ak(C_u + C_d)]/(\mu LC_u C_d) \quad (15)$$

305 with the time ( $t$ ), the cross-sectional area ( $A$ ) and the length ( $L$ ) of the sample, the  
306 viscosity of the pore fluid ( $\mu=10^{-3}$  Pa.s at 20°C), the permeability ( $k$  in  $m^2$ ), and the  
307 compressive storages of the upstream and downstream pore pressure circuits ( $C_u =$   
308  $3.957 \times 10^{-9}$   $m^3/MPa$  and  $C_d = 4.828 \times 10^{-9}$   $m^3/MPa$ , respectively).

309 *Permeability from mercury injection capillary pressure (MICP)*

310 Pore throats size distribution measured by MICP was used to determine Katz-  
311 Thompson permeability  $K_{KT}$  (Katz and Thompson, 1986, 1987; Nishiyama and  
312 Yokoyama, 2014) with Equation (16):

$$313 \quad K_{KT} = \frac{1}{89} \phi_i \frac{(l_i^h)^3}{l_c} f(l_{max}^h) \quad (16)$$

314 with the pore throat diameter ( $l_c$ ) at the inflection point of the cumulative MICP curve  
315  $f(l)$  of fractional volume of connected pore throats with diameters of  $l$  and larger, the  
316 pore throat diameter ( $l_{max}^h$ ) corresponding to the optimum path for permeability when  
317  $l^3 f(l)$  is maximum and  $l = l_{max}^h$  (Katz and Thompson, 1986, 1987).

## 318 **Results**

### 319 ***Site U1517***

320 At Site U1517, CEC is very low to low (~0.05–0.20 mol/kg), independent of  
321 lithological units, and averages 0.15 mol/kg (Figure 4c). The range of CEC values  
322 suggests that the relatively homogeneous (~32%) total clay mineral content across the  
323 section (Figure 4b) is composed of a mix of smectite, illite, kaolinite and or/chlorite. In  
324 particular, the comparison of CEC values measured in siliciclastic clay-rich samples  
325 from the North Sumatra margin (Duttilleul et al., 2020a) and other sites from the North  
326 Hikurangi margin (e.g. Duttilleul et al., 2020b and in press) with the clay mineral  
327 assemblage determined by XRD in near-by samples (e.g. Rosenberger et al., 2020;  
328 Underwood, 2021) suggests that at Site U1517, smectite content in bulk sediment  
329 ranges ~5%-30% (Figure 8). These values agree with the post-cruise XRD  
330 characterisation of the clay mineral assemblage of Underwood and Dugan (2021). This  
331 study shows that smectite and illite contents in bulk sediment range ~5%-29% and

332 ~5%-21% respectively while chlorite and kaolinite contents are <5% and <1%  
333 respectively (S. Cardona, pers. comm.)

334         Consequently, bound water content is low (~2%–8%, ~6% on average) and  
335 relatively homogeneous across the sedimentary section at Site U1517. Hence, total  
336 connected porosity and interstitial porosity show similar variation across the section  
337 drilled, in this case, an overall decrease with increasing depth (Figure 4d). However, no  
338 general compaction trend can be defined at Site U1517. In detail, interstitial porosity  
339 exponentially decreases from ~64% at the seafloor to ~34% at the base of the South  
340 TLC. The interstitial porosity versus vertical effective stress ( $\sigma'_v$ ) curve determined by  
341 least-square fitting is  $\phi_i = 45.6 e^{-0.57\sigma'_v}$  ( $R^2=0.40$ , as shown in Figure 7) for the South TLC  
342 interval. A strong contrast appears with the top of lithological Unit IV where interstitial  
343 porosity is ~45% and decreases with increasing scatter following  $\phi_i = 47.6 e^{-0.14\sigma'_v}$  (least-  
344 square fitting with  $R^2=0.23$ ) down to ~40% at ~185 mbsf. The interstitial porosity tracks  
345 the LWD NMR porosity very well but it does not track the LWD neutron porosity  
346 which shows higher values (Figure 4d). Larger neutron porosity values are typically  
347 detected in clay-rich sediments (e.g. Expedition 314 Scientists, 2009; Expedition 317  
348 Scientists, 2011; Expedition 334 Scientists, 2012a, b; Dutilleul et al., 2020b) due to the  
349 high concentration of hydrogen characterising the hydroxyls of the mineral structure of  
350 the clay, with a possible additional effect of trace elements acting as thermal absorbers  
351 (Ellis, 1986; Ellis and Singer, 2007). NMR porosity measured on samples generally  
352 matches LWD NMR porosity, although the latter  $T_2$  distribution is truncated at values  
353 between 1 and 1000 ms (Barnes et al., 2019b) in contrast to laboratory measurements.  
354 An exception is Unit IV, where NMR porosity tracks LWD neutron porosity.



355 Overall, resistivity-derived porosity fits interstitial porosity with  $a = 1$  and  $m = 1.7$   
356 in the TLC and  $m = 1.9$  below (Figure 4i) except in some intervals (~20–30, ~96–106,  
357 ~135–165 mbsf) as discussed below.

358 Figure 9 shows the permeability data obtained on cores 17H6 and 29F3 under a  
359 constant pore fluid pressure of 8 and 8.5 MPa respectively corresponding to their in-situ  
360 pore pressure conditions and an increasing effective hydrostatic confining pressure from  
361 1 to 20 MPa. The lowest effective pressure is slightly higher than the in-situ pressure for  
362 sample 17H6 (0.87 MPa) and slightly lower for sample 29F3 (1.39 MPa). The  
363 progressive closure of cracks can explain the decrease of permeability  $k$  with effective  
364 pressure  $P_{\text{eff}}$ . Walsh (1981) proposed a fracture closure model that suggests that  $k^{1/3}$   
365 should be linearly related to  $\log P_{\text{eff}}$ . Permeability plotted as  $k^{1/3}$  is shown as a function  
366 of  $P_{\text{eff}}$  in a linear-log graph in Figure 10 for samples 17H6 and 29F3. The data are found  
367 to follow a linear trend, in agreement with Walsh's model. They correspond to the over-  
368 consolidation of the samples with an initially measured permeability ( $1.3 \cdot 10^{-18} \text{ m}^2$  for  
369 core 17H6 and  $1.4 \cdot 10^{-17} \text{ m}^2$  for core 29F3) close to the expected in-situ permeability.

370 MICP shows that the average size of pore throats decreases and is homogenised  
371 with increasing depth from  $0.3 \text{ }\mu\text{m}$  to  $0.1 \text{ }\mu\text{m}$  in lithological Units I to IV (Figure 4e).  
372 Lithological Unit V shows contrasted ranges of pore throat diameters with a general  
373 trend toward higher values, increasing up to  $\sim 1.4 \text{ }\mu\text{m}$  at  $\sim 165$  mbsf, and dropping down  
374 to  $\sim 0.4 \text{ }\mu\text{m}$  in the lower part of the unit (Figures 4e and 11). The corresponding  
375 permeabilities determined using the Katz-Thompson model are in the order of  $10^{-17} \text{ m}^2$ .  
376 These estimated permeability values are somewhat higher than those measured under  
377 in-situ conditions (see, for example, core 17H6). The effective pressure effect may  
378 explain the difference since the Katz-Thompson estimate holds for zero pressure  
379 conditions and permeability has been shown to decrease at pressures lower than our

380 minimum of 1 MPa (Screaton et al., 2021). Another possible explanation may be the  
381 lower water permeability in clay- and silt-rich rocks compared to gas permeability, due  
382 to fluid-rock interactions that the Katz-Thompson model does not consider.

383 NMR  $T_2$  measured on samples and LWD NMR  $T_2$  are both well correlated to the  
384 average size of pore throats but show contrasting values (Figure 4f). NMR  $T_2$  measured  
385 on samples are in the range of ~1–2 ms. In contrast, LWD NMR  $T_2$  decreases from ~20  
386 to ~6 ms from the seafloor to the bottom of Unit IV. It increases up to ~30 ms before  
387 dropping in the lower part of Unit V. The average LWD relaxivity is ~9  $\mu\text{m/s}$  while the  
388 average relaxivity measured on samples is ~50  $\mu\text{m/s}$ .

#### 389 *Site U1519*

390 At Site U1519, CEC is low but in the high range measured at Site U1517  
391 (~0.14–0.20 mol/kg). CEC is also independent of lithological units and averages 0.16  
392 mol/kg (Figure 5c). This range of values suggests that the clay mineral assemblage,  
393 which constitutes ~45% of the bulk mineralogy of sediments, is homogeneous (Figure  
394 5b). Similarly to Site U1517, the CEC values suggest that the clay fraction is composed  
395 of a mix of smectite (~5%-30% based on Figure 8), illite, kaolinite, and or/chlorite  
396 taking into account that CEC and XRD measurements were not carried out on the same  
397 samples, resulting in significant scattering ( $\pm 15\%$ ). This result cannot be confirmed  
398 since no characterisation of the clay mineral assemblage was undertaken at Site U1519.

399 The resulting bound water content is low (~5%–8%) and relatively  
400 homogeneous across the section, averaging 7%. Hence, as observed at Site U1517, total  
401 connected porosity and interstitial porosity vary similarly (Figure 5d). Across the  
402 limited intervals where coring was attempted, the interstitial porosity decreases with  
403 increasing depth from 68% below the seafloor to ~33% at the bottom of Unit I, it shows  
404 slightly lower values at the bottom of logging and seismic Units 2 (~31%) before

405 increasing across logging and seismic Units 3 up to ~ 35% with a maximum ~42%  
406 around 605 mbsf. In the first unit, strong porosity contrast occurs based on grain size,  
407 with a general trend toward higher porosity values (+5% in average) in mudstones than  
408 in shallower clayey siltstones/silty claystones. In contrast to Site U1517, the interstitial  
409 porosity at Site U1519 is in better agreement with the LWD neutron porosity than with  
410 the NMR porosity, which shows lower values. The NMR porosity measured on samples  
411 exceeds the LWD NMR porosity and matches both interstitial and LWD neutron  
412 porosities.

413         The resistivity-derived porosity fits the interstitial and onboard interstitial  
414 porosities with  $a = 1$  and  $m = 1.9$  in lithological Unit I,  $m = 2.3$  in the lower part of  
415 seismic and logging Units 2 (top of lithological Unit II), and  $m = 2.6$  in the top of  
416 logging and seismic Units 3 (bottom of Unit II) except in a zone ~600–620 mbsf (Figure  
417 5i). A general compaction trend  $\phi_i = 39.3 e^{-0.03\sigma'_v}$  ( $R^2 = 0.16$ ) can be defined at Site U1519  
418 (excluding the washout interval ~148-227 mbsf) based on fitting the resistivity-derived  
419 porosity to the onboard interstitial porosity. In detail, three different compaction trends  
420 can be defined to best fit the data (Figure 7): the first one for clayey siltstones/silty  
421 claystones in lithological Unit I, the second one for mudstones of the same unit, and the  
422 third one for Unit II. We notice that the compaction trend for shallow clayey  
423 siltstones/silty claystones in Unit I at Site U1519 determined from the onboard  
424 interstitial porosity is equivalent to that of the TLC at Site U1517 where the same type  
425 of lithology or even coarser lithologies have been identified.

426         MICP shows that the average size of pore throat diameters decreases and  
427 becomes more homogeneous with increasing depth from ~0.45  $\mu\text{m}$  to ~0.15  $\mu\text{m}$  near the  
428 bottom of the hole (Figures 5e and 11). As observed at Site U1517, the permeabilities  
429 determined using the Katz-Thompson model are in the order of  $10^{-17} \text{ m}^2$ . NMR  $T_2$

430 measured on samples and LWD NMR  $T_2$  show diverging values ( $\sim 10$ – $2.30$  ms and  
431  $\sim 19$ – $3$  ms, respectively), although their evolution correlates with that of the average  
432 pore throat size measured by MICP (Figure 5e; f). The average LWD relaxivity is  $\sim 14$   
433  $\mu\text{m/s}$  while the average relaxivity measured on samples is  $\sim 90$   $\mu\text{m/s}$ .

## 434 **Discussion**

### 435 *Physical properties of gas hydrates bearing intervals*

436 When not directly observed onboard, gas hydrate occurrence (green rectangle  
437 and shaded zones in Figure 4 and green rectangle in Figure 5) was inferred from 1)  
438 negative anomaly of pore water content (Figures 4j et 5j) due to gas hydrate dissociation  
439 during core retrieval (Paull and Ussler, 2001), or 2) positive peaks of LWD P-wave  
440 velocity (Figures 4g and 5g) and resistivity (Figures 4h and 5h) (Barnes et al., 2019b).  
441 However, there are uncertainties regarding the precise location of gas hydrate-bearing  
442 intervals estimated from the salinity detection method. Indeed, other phenomena,  
443 including changes in the salinity of the water mass, diagenetic reactions or the pore  
444 water extraction method used onboard may also cause negative chloride anomalies  
445 (Fitts and Brown, 1999; Barnes et al., 2019b, c; Sultan, 2020). At Site U1517, chloride  
446 data mark a zone in the preslide interval among  $\sim 135$  and  $\sim 165$  mbsf with gas hydrate  
447 saturation ranging 2%–68% (Barnes et al., 2019b), with the BGHS at  $\sim 162$  mbsf  
448 (Screaton et al., 2019) (Figure 4). Sultan (2020) reinterpreted chloride anomalies and  
449 proposed a BGHS between 85 and 128 mbsf, although this is not supported by Screaton  
450 et al. (2019, 2020). LWD data evidenced three intervals potentially hosting gas hydrates  
451 (green shaded zones on Figure 4) between  $\sim 112$ – $114$ ,  $\sim 117$ – $121$  and  $\sim 128$ – $145$  mbsf  
452 (Barnes et al., 2019b). At Site U1519, chloride data mark a damage zone (Figure 5k)  
453 between 520 and 630 mbsf with elevated gas hydrate concentration with a discrete

454 negative anomaly ~628 mbsf (Figure 5j) where the occurrence of gas hydrates has been  
455 directly evidenced by core IR scanning in silt layers with higher CEC at ~627 mbsf.

456 Gas hydrate distribution depends on the initial characteristics of the porous  
457 medium and the effective stress that control the growing space, thus porosity and  
458 permeability (Dai et al., 2012, He et al., 2013) which vary with hydrate formation and  
459 dissociation (Misyura, 2016; Wang, 2020). When hydrates form in the pore space, the  
460 permeability of gas hydrate saturated sediments decreases (Nimblett and Ruppel, 2003;  
461 Dai and Seol, 2014; Daigle et al., 2015b; Wei et al., 2021) while it increases when  
462 hydrates dissociate (Wang, 2020). Sediments characterised by a high initial porosity are  
463 more sensitive to permeability changes associated with increasing gas hydrates  
464 saturation (Shen et al., 2020).

465 Although there are uncertainties concerning the precise location of gas hydrate-  
466 bearing intervals (e.g. Barnes et al., 2019b, c; Sreaton et al., 2019 and 2020; Sultan,  
467 2020), our core-based dataset shows evidence that the sediment matrix in intervals  
468 likely to host gas hydrates, as inferred from chloride anomalies, is characterised by a  
469 general trend of higher interstitial porosities, average pore diameters, and Katz-  
470 Thompson permeabilities (Figures 4 and 5). These characteristics are favorable to the  
471 growth of gas hydrates. This behaviour is more visible at Site U1517 (~135-160 mbsf)  
472 than at Site U1519 (~520-630 mbsf). On LWD data, intervals hosting gas hydrates are  
473 typically characterised by high electrical resistivity (Goldberg et al., 2010) and P-wave  
474 velocity (Waite et al., 2009) values and apparent lower NMR porosity (Kleinberg,  
475 2003). Similar values, for zones thought to host gas hydrates, can be observed at Site  
476 U1517 in the intervals between ~112–114, ~117–121 and ~128–145 mbsf or in some  
477 intervals at the meter scale between ~135 and 160 mbsf at Site U1517 (Figure 4h) and  
478 ~520-630 mbsf at Site U1519 (Figure 5h).

479 ***Overview of the compaction state and creep mechanisms at the South TLC***

480 Several zones at both sites show anomalously high values of resistivity-derived  
481 porosity relative to the compaction curve or the onboard interstitial porosity. Two  
482 intervals at Site U1517 (~20–30 mbsf and ~96–106 mbsf) and one at Site U1519 (~148–  
483 227 mbsf) represented by the grey shaded zones in Figures 4 and 5 with anomalously  
484 high resistivity-derived porosity correspond to washout zones (Barnes et al., 2019b, c).  
485 Peaks of high resistivity-derived porosity related to the occurrence of gas hydrates in the  
486 pore space also occur in the zone ~135-165 mbsf at Site U1517. In this section, the  
487 rapid dissociation of gas hydrates when cores are brought to the surface results in the  
488 freshening of the pore water extracted from cores, impacting resistivity-derived porosity  
489 (Barnes et al., 2019b) (Figures 4j and 5j). These zones excluded, interstitial porosity or  
490 resistivity-derived porosity can be examined to determine compaction state and discuss  
491 mechanisms behind creeping at the South TLC.

492 At Site U1517, interstitial porosity versus effective vertical stress curve (referred  
493 to as compaction trend) and cementation factor  $m$  vary across the TLC (~0-67 mbsf)  
494 and in the preslide interval beneath (Figure 7). In particular, although Units II and III  
495 (considered here as corresponding to the upper and lower units of the landslide) may not  
496 be genetically linked and show variations in lithology and emplacement mechanisms  
497 (Gross et al., 2018; Couvin et al., 2020; Luo et al., 2020), their porosity values plot on  
498 the same compaction trend (Figure 7). This compaction trend is similar to that of the  
499 upper sedimentary section at Site U1519, at Site U1518 nearby the deformation front  
500 (Dutilleul et al., in press), and at Site U1520 in the Hikurangi Trough (Dutilleul et al.,  
501 2020b). This suggests that mechanical compaction of shallow poorly consolidated  
502 sediments is relatively uniform across the margin, although siliciclastic lithology may  
503 slightly vary in terms of grain size between these different locations. The ‘negative

504 polarity intra-debris reflector' at the interface between Units II and III identified by  
505 Gross et al. (2018) (~37 mbsf, marker D in Figure 4) is not associated with an  
506 anomalously high interstitial porosity nor resistivity-derived porosity. Such anomaly  
507 was expected since this reflector has been inferred to represent an excess pore pressure  
508 zone (Gross et al., 2018) coinciding with the décollement for active creeping (Barnes et  
509 al., 2019a, b).

510         However, onboard interstitial porosity increases by 11% and resistivity-derived  
511 porosity by 7% at the base of the landslide at Site U1517 (~67 mbsf, marker B in Figure  
512 4). Three hypotheses can explain the distinct porosity patterns observed in the landslide  
513 and the preslide intervals with strong porosity shift at the interface:

- 514         • Hypothesis 1: a local excess pore pressure.
- 515         • Hypothesis 2: differences in lithology, emplacement mechanisms, and  
516             deformation history result in distinct compaction trends in the landslide and  
517             preslide intervals.
- 518         • Hypothesis 3: a combination of hypotheses 1 and 2.

519 Hypothesis 1 is supported by the rapid burial of sediment due to the emplacement of the  
520 landslide (Screaton et al., 2019), which is likely to release fluids through rapid  
521 compaction of the preslide interval. Although our dataset does not clearly show a  
522 contrast of permeability at the base of the landslide, the clay-rich upper part of the  
523 preslide interval is prone to the accumulation of the released fluids, thus to excess pore  
524 pressure development which may also be triggered by focused fluid flow (Carey et al.,  
525 2019). On the other hand, the lithology contrast between the landslide, characterised by  
526 numerous sand and silt-rich turbidites, and the clay-rich upper part of the preslide  
527 interval supports hypothesis 2 (Gamage et al., 2011). Hypothesis 2 is also supported by  
528 the strong differences in emplacement mechanisms and thus the deformation history of

529 the preslide interval characterised by a mixed slope sedimentary succession (Barnes et  
530 al., 2019b) and the landslide interval. As a consequence of the quick deposition of the  
531 landslide, the preslide interval should be more consolidated than the lower landslide  
532 unit. In fact, it is less consolidated, which supports hypothesis 1. Hence, we suggest that  
533 hypothesis 3 is the most plausible.

534 IODP Expedition 372 drilling results and Screatton et al. (2019) have shown that gas  
535 hydrates are not involved in active creeping at the South TLC interval where they are  
536 absent. In the preslide interval where gas hydrates are expected to occur, the lack of  
537 excess pore pressure at the BGHS, evidenced by our dataset, shows that neither the  
538 hydrate dissociation model nor the hydrate pressure valve model, linking gas hydrates to  
539 slow deformation, is possible. The results of this study allow the examination of  
540 mechanisms, which are not related to gas hydrates, but may explain active creeping in  
541 the South TLC interval. Our findings support the repeated small-scale failure  
542 mechanism associated with cycles of excess pore pressure as initially proposed by  
543 Mountjoy et al. (2009), since no (hypothesis 2) or moderate (hypotheses 1 and 3) excess  
544 pore pressure is found at Site U1517 in the extensional zone of the South TLC. This  
545 mechanism could be validated in the case that a larger excess pore pressure is evidenced  
546 in the compressional zone of the landslide, which has not yet been drilled (Barnes et al.,  
547 2019a).

548 The sedimentary section at Site U1519 is in hydrostatic conditions. However, ~600  
549 mbsf (~5.9 MPa in Figure 7), there is a zone where onboard interstitial porosity is 4–  
550 11% higher than the value predicted by the compaction curve of Unit II. This  
551 discrepancy of porosity values could be related to an excess pore pressure in the order  
552 of ~1.5–5 MPa. The origin of this potential excess pore pressure zone is unclear. It  
553 could be related to concentrated fluid flow in a high permeability sand-rich interval



554 sandwiched between lower permeability MTDs. Another possibility is a relation  
555 between the presence of free gas and the nearby location of the BGHS. However, the  
556 latter is not well constrained with, on the one hand, a possible BSR ~560 mbsf or below,  
557 and on the other hand, gas hydrates sampled in a core at ~627 mbsf (Pecher et al.,  
558 2019c).

## 559 **Conclusions**

560 We quantify interstitial porosity at the south (Site U1517) and the north (Site  
561 U1519) TLC by correcting the total connected porosity measured on core samples for  
562 bound water content determined from cation exchange capacity. At Site U1517,  
563 interstitial porosity decreases by ~30% across the TLC (~64–34%), following a  
564 compaction trend different from that of the preslide interval beneath. This porosity  
565 decrease is associated with a reduction of pore throats from ~0.3 to ~0.1  $\mu\text{m}$ . At Site  
566 U1519 where coring was limited, we use the interstitial porosity to calibrate the high-  
567 resolution resistivity-derived porosity. It decreases from ~68% to ~42% following three  
568 different compaction trends, corresponding to a reduction in the average size of pore  
569 throats from ~0.45 to ~0.15  $\mu\text{m}$  across the sedimentary section. At both sites, the in-situ  
570 permeability measured with a triaxial cell and deduced from pore size measurements  
571 ranges from  $10^{-18}$  to  $10^{-17}$   $\text{m}^2$ . The dataset shows that the sedimentary intervals suspected  
572 to host gas hydrates ~112–114, ~117–121 and ~128–145 and ~135 and 160 mbsf at Site  
573 U1517 and between ~520 and 630 mbsf at Site U1519 exhibit higher interstitial  
574 porosity, pore diameter and permeability favorable to the growth of gas hydrates. These  
575 results suggest hydrostatic conditions across most of the two sedimentary sections.  
576 However, at Site U1519, excess pore pressure may occur in a zone below the base of the  
577 gas hydrate stability zone. At Site U1517, a porosity shift of ~+10% occurs at the base  
578 of the landslide. We suggest that this substantial difference in the porosity profile

579 between the landslide and preslide intervals results from a combination of 1) contrasted  
580 physical properties due to differences in lithology, emplacement mechanisms and  
581 compaction history and 2) moderate excess pore pressure associated with the trapping of  
582 fluids at the base of the landslide. The results of IODP Expedition 372 discredit the role  
583 of gas hydrates in active creeping at the TLC. Our results open the way to the study of  
584 other mechanisms at the TLC, such as potentially repeated small-scale failure associated  
585 with charge and discharge of excess pore pressure, or at analogous basins where  
586 submarine landslides and gas hydrates coexist. Future work, such as in situ pore  
587 pressure analysis recorded at Site U1519, is required to understand the mechanisms of  
588 creep at the TLC.

#### 589 **Acknowledgements**

590 This study and the shore-based measurements were funded by CNRS-INSU and  
591 IODP-France, which we greatly acknowledge. The complete crews of IODP  
592 Expeditions 372 and 375 are sincerely thanked. We also thank David Billet, Philippe  
593 Rousselle, Maximilien Beuret and Géraldine Kitzinger from the LIEC laboratory in  
594 Nancy and Metz (France) for running CEC, exchangeable cation composition and  
595 soluble chloride content analyses. We thank Khalid Essa for his support in proofreading  
596 the manuscript. We finally thank Ann Cook and Sebastian Cardona for their very  
597 constructive reviews that greatly improved this manuscript as well as Adam McArthur  
598 for editorial handling.

#### 599 **Data**

600 This research used data provided by the International Ocean Discovery Program  
601 (IODP) and freely available on the LIMS Report Interface Page at  
602 [web.iodp.tamu.edu/LORE](http://web.iodp.tamu.edu/LORE) or on the log database at

603 [mlp.ldeo.columbia.edu/logdb/scientific\\_ocean\\_drilling](http://mlp.ldeo.columbia.edu/logdb/scientific_ocean_drilling). Post-cruise data including  
604 corrected porosity, CEC, exchangeable cation composition, MICP and NMR are  
605 available in the OTELo Research Data Repository ([https://doi.org/10.24396/ORDAR-](https://doi.org/10.24396/ORDAR-40)  
606 [40](https://doi.org/10.24396/ORDAR-40) for Site U1519 and <https://doi.org/10.24396/ORDAR-41> for Site U1517).

## 607 **References**

- 608 Alexander CR, Walsh JP, Orpin AR. 2010. Modern sediment dispersal and  
609 accumulation on the outer Poverty continental margin. *Marine Geology*.  
610 270(1):213–226. <https://doi.org/10.1016/j.margeo.2009.10.015>
- 611 Archie, G E. 1942. The electrical resistivity log as an aid in determining some reservoir  
612 characteristics. *Transactions of the American Institute of Mining Metallurgical*  
613 *and Petroleum Engineers* (146):54-62. <https://doi.org/10.2118/942054-G>
- 614 Barnes PM, Cheung KC, Smits AP, Almagor G, Read SAL, Barker PR, Froggatt P.  
615 1991. Geotechnical analysis of the kidnappers slide, upper continental slope,  
616 New Zealand. 10(1–2):159–188. <https://doi.org/10.1080/10641199109379888>
- 617 Barnes PM, Nicol A, Harrison T. 2002. Late Cenozoic evolution and earthquake  
618 potential of an active listric thrust complex above the Hikurangi subduction  
619 zone, New Zealand. *GSA Bulletin*. 114(11):1379–1405.  
620 [https://doi.org/10.1130/0016-7606\(2002\)114<1379:LCEAEP>2.0.CO;2](https://doi.org/10.1130/0016-7606(2002)114<1379:LCEAEP>2.0.CO;2)
- 621 Barnes PM, Pecher IA, LeVay LJ, Bourlange SM, Brunet MMY, Cardona S, Clennell  
622 MB, Cook AE, Crundwell MP, Dugan B, Elger J, Gamboa D, Georgiopoulou A,  
623 Greve A, Han S, Heeschen KU, Hu G, Kim GY, Kitajima H, Koge H, Li X,  
624 Machado KS, McNamara DD, Moore GF, Mountjoy JJ, Nole MA, Owari S,  
625 Paganoni M, Petronotis KE, Rose PS, Sreaton EJ, Shankar U, Shepherd CL,  
626 Torres ME, Underwood MB, Wang X, Woodhouse AD, Wu H-Y. 2019a.  
627 Expedition 372A summary. In Pecher IA, Barnes PM, LeVay LJ and the  
628 Expedition 372A Scientists, *Creeping Gas Hydrate Slides*. Proceedings of the  
629 International Ocean Discovery Program, 372A: College Station, TX  
630 (International Ocean Discovery Program), [https://doi.org/10.14379/](https://doi.org/10.14379/iodp.proc.372A.101.2019)  
631 [iodp.proc.372A.101.2019](https://doi.org/10.14379/iodp.proc.372A.101.2019)
- 632 Barnes PM, Pecher IA, LeVay LJ, Bourlange SM, Brunet MMY, Cardona S, Clennell  
633 MB, Cook AE, Crundwell MP, Dugan B, Elger J, Gamboa D, Georgiopoulou A,

634 Greve A, Han S, Heeschen KU, Hu G, Kim GY, Kitajima H, Koge H, Li X,  
635 Machado KS, McNamara DD, Moore GF, Mountjoy JJ, Nole MA, Owari S,  
636 Paganoni M, Petronotis KE, Rose PS, Screamon EJ, Shankar U, Shepherd CL,  
637 Torres ME, Underwood MB, Wang X, Woodhouse AD, Wu H-Y. 2019b. Site  
638 U1517. In Pecher IA, Barnes PM, LeVay LJ and the Expedition 372A Scientists,  
639 Creeping Gas Hydrate Slides. Proceedings of the International Ocean Discovery  
640 Program, 372A: College Station, TX (International Ocean Discovery Program),  
641 <https://doi.org/1014379/iodpproc372A1032019>

642 Barnes PM, Wallace LM, Saffer DM, Pecher IA, Petronotis KE, LeVay LJ, Bell RE,  
643 Crundwell MP, Engelmann de Oliveira CH, Fagereng A, Fulton PM, Greve A,  
644 Harris RN, Hashimoto Y, Hüpers A, Ikari MJ, Ito Y, Kitajima H, Kutterolf S,  
645 Lee H, Li X, Luo M, Malie PR, Meneghini F, Morgan JK, Noda A, Rabinowitz  
646 HS, Savage HM, Shepherd CL, Shreedharan S, Solomon EA, Underwood MB,  
647 Wang M, Woodhouse AD, Bourlange SM, Brunet MMY, Cardona S, Clennell  
648 MB, Cook AE, Dugan B, Elger J, Gamboa D, Georgiopoulou A, Han S,  
649 Heeschen KU, Hu G, Kim GY, Koge H, Machado KS, McNamara DD, Moore  
650 GF, Mountjoy JJ, Nole MA, Owari S, Paganoni M, Rose PS, Screamon EJ,  
651 Shankar U, Torres ME, Wang X, Wu H-Y. 2019c. Site U1519. In Wallace LM,  
652 Saffer DM, Barnes PM, Pecher IA, Petronotis KE, LeVay LJ, and the  
653 Expedition 372/375 Scientists. Hikurangi Subduction Margin Coring, Logging,  
654 and Observatories Proceedings of the International Ocean Discovery Program,  
655 372B/375: College Station, TX (International Ocean Discovery Program),  
656 <https://doi.org/1014379/iodpproc372B3751042019>

657 Bertrand L, Géraud Y, Diraison M. (2021). Petrophysical properties in faulted basement  
658 rocks: Insights from outcropping analogues on the West European Rift  
659 shoulders. *Geothermics*. 95 (102144).  
660 <https://doi.org/10.1016/j.geothermics.2021.102144>

661 Blum P. 1997. Physical properties handbook: a guide to the shipboard measurement of  
662 physical properties of deep-sea cores. ODP Tech. Note, 26. [http://www-](http://www-odp.tamu.edu/publications/tnotes/tn26/INDEX.HTM)  
663 [odp.tamu.edu/publications/tnotes/tn26/INDEX.HTM](http://www-odp.tamu.edu/publications/tnotes/tn26/INDEX.HTM)

664 Bossennec C, Géraud Y, Moretti I, Mattioni L, Stemmelen D. 2018. Pore network  
665 properties of sandstones in a fault damage zone. *Journal of Structural Geology*.  
666 110:24–44. <https://doi.org/10.1016/j.jsg.2018.02.003>

- 667 Böttner C, Gross F, Geersen J, Crutchley GJ, Mountjoy JJ, Krastel S. 2018. Marine  
668 Forearc Extension in the Hikurangi Margin: New Insights From High-  
669 Resolution 3-D Seismic Data. *Tectonics*. 37(5):1472–1491.  
670 <https://doi.org/10.1029/2017TC004906>
- 671 Bourlange S, Henry P, Moore JC, Mikada H, Klaus A. 2003. Fracture porosity in the  
672 décollement zone of Nankai accretionary wedge using Logging While Drilling  
673 resistivity data. *Earth and Planetary Science Letters*. 209(1–2):103–112.  
674 [https://doi.org/10.1016/S0012-821X\(03\)00082-7](https://doi.org/10.1016/S0012-821X(03)00082-7)
- 675 Brown KM, Ransom B. 1996. Porosity corrections for smectite-rich sediments: Impact  
676 on studies of compaction, fluid generation, and tectonic history. *Geology*.  
677 24(9):843–846. [https://doi.org/10.1130/0091-  
678 7613\(1996\)024<0843:PCFSRS>2.3.CO;2](https://doi.org/10.1130/0091-7613(1996)024<0843:PCFSRS>2.3.CO;2)
- 679 Bussian AE. 1983. Electrical conductance in a porous medium. *Geophysics*.  
680 48(9):1258–1268. <https://doi.org/10.1190/1.1441549>
- 681 Brace WF. 1984. Permeability of crystalline rocks: new in situ measurements. *Journal*  
682 *of Geophysical Research: Solid Earth*. 89(B6):4327–4330.  
683 <https://doi.org/10.1029/JB089iB06p04327>
- 684 Canals M, Lastras G, Urgeles R, Casamor JL, Mienert J, Cattaneo A, De Batist M,  
685 Haflidason H, Imbo Y, Laberg JS, Locat J, Long D, Longva O, Masson DG,  
686 Sultan N, Trincardi R, Bryn P. 2004. Slope failure dynamics and impacts from  
687 seafloor and shallow sub-seafloor geophysical data: case studies from the  
688 COSTA project. *COSTA - Continental Slope Stability* 213(1):9-72.  
689 <https://doi.org/10.1016/j.margeo.2004.10.001>
- 690 Carey JM, Crutchley GJ, Mountjoy JJ, Petley DN, McSaveney MJ, Lyndsell B. 2019.  
691 Slow episodic movement driven by elevated pore-fluid pressures in shallow  
692 subaqueous slopes. *Geomorphology*. 329:99–107.  
693 <https://doi.org/10.1016/j.geomorph.2018.12.034>
- 694 Carr HY, Purcell EM. 1954. Effects of diffusion on free precession in nuclear magnetic  
695 resonance experiments. *Physical Review*. 94(3):630–638.  
696 <https://doi.org/10.1103/PhysRev.94.630>
- 697 Conin M, Henry P, Bourlange S, Raimbourg H, Reuschlé T. 2011. Interpretation of  
698 porosity and LWD resistivity from the Nankai accretionary wedge in light of

699 clay physicochemical properties: Evidence for erosion and local overpressuring.  
700 Geochemistry, Geophysics, Geosystems. 12(3).  
701 <https://doi.org/10.1029/2010GC003381>

702 Couvin B, Georgiopoulou A, Mountjoy JJ, Amy L, Crutchley GJ, Brunet M, Cardona S,  
703 Gross F, Böttner C, Krastel S, Pecher I. 2020. A new depositional model for the  
704 Tuaheni Landslide Complex, Hikurangi Margin, New Zealand. Geological  
705 Society, London, Special Publications. 500(1):551–566.  
706 <https://doi.org/10.1144/SP500-2019-180>

707 Dai S, Santamarina JC, Waite WF, Kneafsey TJ. 2012. Hydrate morphology: Physical  
708 properties of sands with patchy hydrate saturation, Journal of Geophysical  
709 Research: Solid Earth. 117(B11205). <https://doi.org/10.1029/2012JB009667>.

710 Dai S, Seol Y. 2014. Water permeability in hydrate-bearing sediments: a pore-scale  
711 study. Geophysical Research Letters. 41(12): 4176–4184.  
712 <https://doi.org/10.1002/2014GL060535>

713 Daigle H, Thomas B, Rowe H, Nieto M. 2014. Nuclear magnetic resonance  
714 characterization of shallow marine sediments from the Nankai Trough,  
715 Integrated Ocean Drilling Program Expedition 333: NMR of Nankai Trough  
716 sediments. Journal of Geophysical Research: Solid Earth. 119(4):2631–2650.  
717 <https://doi.org/10.1002/2013JB010784>

718 Daigle H, Ghanbarian B, Henry P, Conin M. 2015a. Universal scaling of the formation  
719 factor in clays: Example from the Nankai Trough. Journal of Geophysical  
720 Research: Solid Earth. 120(11):7361–7375.  
721 <https://doi.org/10.1002/2015JB012262>

722 Daigle H, Cook A, Malinverno A. 2015b. Permeability and porosity of hydrate-bearing  
723 sediments in the northern Gulf of Mexico. Marine and Petroleum Geology.  
724 68(A):551-564. <https://doi.org/10.1016/j.marpetgeo.2015.10.004>

725 Dutilleul J, Bourlange S, Conin M, Géraud Y. 2020. Quantification of bound water  
726 content, interstitial porosity and fracture porosity in the sediments entering the  
727 North Sumatra subduction zone from Cation Exchange Capacity and IODP  
728 Expedition 362 resistivity data. Marine and Petroleum Geology. 111:156–165.  
729 <https://doi.org/10.1016/j.marpetgeo.2019.08.007>

730 Dutilleul J, Bourlange S, Géraud Y, Stemmelen D. 2020. Porosity, Pore Structure, and  
731 Fluid Distribution in the Sediments Entering the Northern Hikurangi Margin,

732 New Zealand. *Journal of Geophysical Research: Solid Earth*. 125(11).  
733 <https://doi.org/10.1029/2020JB020330>

734 Dutilleul J, Bourlange S, Geraud Y. In Press. Porosity and compaction state at the active  
735 Pāpaku thrust fault in the frontal accretionary wedge of the Northern Hikurangi  
736 margin. *Geochemistry, Geophysics, Geosystems*.  
737 <https://doi.org/10.1029/2020GC009325>

738 Ellis DV. 1986. Neutron porosity devices—what do they measure? *First Break*.4(3):11–  
739 17. <https://doi.org/10.3997/1365-2397.1986005>

740 Ellis DV, Singer JM. 2007. *Well logging for earth scientists*. 2nd ed. Dordrecht, The  
741 Netherlands: Springer.

742 Expedition 314 Scientists, 2009. Expedition 314 Site C0002. In Kinoshita, M., Tobin,  
743 H., Ashi, J., Kimura, G., Lallemand, S., Screaton, E.J., Curewitz, D., Masago, H.,  
744 Moe, K.T., and the Expedition 314/315/316 Scientists, *Proc. IODP*,  
745 314/315/316: Washington, DC (Integrated Ocean Drilling Program Management  
746 International, Inc.). <https://doi.org/10.2204/iodp.proc.314315316.114.2009>

747 Expedition 317 Scientists, 2011. Site U1352. In Fulthorpe, C.S., Hoyanagi, K., Blum,  
748 P., and the Expedition 317 Scientists, *Proc. IODP*, 317: Tokyo (Integrated  
749 Ocean Drilling Program Management International, Inc.).  
750 <https://doi.org/10.2204/iodp.proc.317.104.2011>

751 Expedition 334 Scientists, 2012a. Site U1378. In Vannucchi, P., Ujiie, K., Stroncik, N.,  
752 Malinverno, A., and the Expedition 334 Scientists, *Proc. IODP*, 334: Tokyo  
753 (Integrated Ocean Drilling Program Management International, Inc.).  
754 <https://doi.org/10.2204/iodp.proc.334.103.2012>

755 Expedition 334 Scientists, 2012b. Site U1379. In Vannucchi, P., Ujiie, K., Stroncik, N.,  
756 Malinverno, A., and the Expedition 334 Scientists, *Proc. IODP*, 334: Tokyo  
757 (Integrated Ocean Drilling Program Management International, Inc.).  
758 <https://doi.org/10.2204/iodp.proc.334.104.2012>

759 Field BD, Uruski CI, Beu AG, Browne GH, Crampton JS, Funnell RH, Killops SD,  
760 Laird M, Mazengarb C, Morgans HEG, Rait GJ, Smale D, Strong CP. 1997.  
761 *Cretaceous-Cenozoic geology and petroleum systems of the East Coast region*,  
762 New Zealand. Lower Hutt: Institute of Geological & Nuclear Sciences. Institute  
763 of Geological & Nuclear Sciences monograph 19 2 v.

- 764 Fitts TG, Brown KM. 1999. Stress-induced smectite dehydration: ramifications for  
765 patterns of freshening and fluid expulsion in the N. Barbados accretionary  
766 wedge. *Earth and Planetary Science Letters*. 172(1–2):179–197.  
767 [https://doi.org/10.1016/S0012-821X\(99\)00168-5](https://doi.org/10.1016/S0012-821X(99)00168-5)
- 768 Freed R, Peacor D. 1989. Geopressured Shale and Sealing Effect of Smectite to Illite  
769 Transition. *AAPG Bulletin* 73: 1223-1232.
- 770 Gamage K, Sreaton, E, Bekins B, Aiello I. 2011. Permeability–porosity relationships  
771 of subduction zone sediments. *Marine Geology*. 279: 19-36.  
772 <https://doi.org/10.1016/j.margeo.2010.10.010>.
- 773 Goldberg D, Kleinberg R, Weinberger J, Malinverno A, McLellan P, Collett T. 2010.  
774 16. Evaluation of natural gas-hydrate systems using borehole logs, in  
775 *Geophysical Characterization of Gas Hydrates*, edited by M. Riedel, E. C.  
776 Willoughby, and S. Chopra, pp. 239–261, Society of Exploration Geophysicists,  
777 Tulsa, Okla.
- 778 Gross F, Mountjoy JJ, Crutchley GJ, Böttner C, Koch S, Bialas J, Pecher I, Woelz S,  
779 Dannowski A, Micallef A, et al. 2018. Free gas distribution and basal shear zone  
780 development in a subaqueous landslide – Insight from 3D seismic imaging of  
781 the Tuaheni Landslide Complex, New Zealand. *Earth and Planetary Science  
782 Letters*. 502:231–243. <https://doi.org/10.1016/j.epsl.2018.09.002>
- 783 He J, Liu X, Yu Z et al. 2013. Factors influencing the porosity of gas hydrate bearing  
784 sediments. *Science China Earth Sciences*. 56:557–567. [https://doi-org.bases-  
785 doc.univ-lorraine.fr/10.1007/s11430-012-4452-x](https://doi-org.bases-doc.univ-lorraine.fr/10.1007/s11430-012-4452-x)
- 786 Henry P. 1997. Relationship between Porosity, Electrical Conductivity, and Cation  
787 Exchange Capacity in Barbados wedge Sediments. *Proceedings of the Ocean  
788 Drilling Program, Scientific Results*. 156:137-150  
789 <https://doi.org/10.2973/odp.proc.sr.156.020.1997>.
- 790 Henry P, Bourlange S. 2004. Smectite and fluid budget at Nankai ODP sites derived  
791 from cation exchange capacity. *Earth and Planetary Science Letters*. 219(1–  
792 2):129–145. [https://doi.org/10.1016/S0012-821X\(03\)00694-0](https://doi.org/10.1016/S0012-821X(03)00694-0)
- 793 Hsieh PA, Tracy JV, Neuzil CE, Bredehoeft JD, Silliman SE. 1981. A transient  
794 laboratory method for determining the hydraulic properties of ‘tight’ rocks—I.  
795 Theory. *International Journal of Rock Mechanics and Mining Sciences &*



796 Geomechanics Abstracts. 18(3):245–252. <https://doi.org/10.1016/0148->  
797 [9062\(81\)90979-7](https://doi.org/10.1016/0148-9062(81)90979-7)

798 Kastner M, Solomon EA, Harris RN, Torres ME. 2014. Chapter 4.4.3 - Fluid Origins,  
799 Thermal Regimes, and Fluid and Solute Fluxes in the Forearc of Subduction  
800 Zones. In: Stein R, Blackman DK, Inagaki F, Larsen H-C, editors.  
801 Developments in Marine Geology. Vol. 7. Elsevier; p. 671–733.  
802 <https://doi.org/10.1016/B978-0-444-62617-2.00022-0>

803 Katz AJ, Thompson AH. 1986. Quantitative prediction of permeability in porous rock.  
804 Physical Review B. 34(11):8179–8181.  
805 <https://doi.org/10.1103/PhysRevB.34.8179>

806 Katz AJ, Thompson AH. 1987. Prediction of rock electrical conductivity from mercury  
807 injection measurements. Journal of Geophysical Research. 92(B1):599.  
808 <https://doi.org/10.1029/JB092iB01p00599>

809 Kleinberg RL, Flaum C, Straley, C, Brewer, PG, Malby, GE, Peltzer, ET, III,  
810 Freiderich, G, Yesinowski, JP, 2003. Seafloor nuclear magnetic resonance assay of  
811 methane hydrate in sediment and rock. Journal of Geophysical Research: Solid Earth,  
812 108(B3):2137. <https://doi.org/10.1029/2001JB000919>

813 Kuhlmann J, Orpin AR, Mountjoy JJ, Crutchley GJ, Henrys S, Lunenburg R, Huhn K.  
814 2019. Seismic and lithofacies characterization of a gravity core transect down  
815 the submarine Tuaheni Landslide Complex, NE New Zealand. Geological  
816 Society, London, Special Publications. 477(1):479–495.  
817 <https://doi.org/10.1144/SP477.37>

818 Luo M, Torres ME, Kasten S, Mountjoy JJ. 2020. Constraining the Age and Evolution  
819 of the Tuaheni Landslide Complex, Hikurangi Margin, New Zealand, Using  
820 Pore-Water Geochemistry and Numerical Modeling. Geophysical Research  
821 Letters. 47(11). <https://doi.org/10.1029/2020GL087243>

822 Marschall D, Gardner JS, Mardon D, Coates R. 1995. Method for Correlating NMR  
823 Relaxometry and Mercury injection Data. Paper Number 9511 presented at:  
824 SCA Conference.

825 McNeill LC, Dugan B, Petronotis KE, Backman J, Bourlange S, Chemale F, Chen W,  
826 Colson TA, Frederik MCG, Guèrin G, Hamahashi M, Henstock T, House BM,  
827 Hüpers A, Jeppson TN, Kachovich S, Kenigsberg AR, Kuranaga M, Kutterolf S,

828 Milliken KL, Mitchison FL, Mukoyoshi H, Nair N, Owari S, Pickering KT,  
829 Poudoux HFA, Yehua S, Song I, Torres ME, Vannucchi P, Vrolijk PJ, Yang  
830 T, Zhao X, 2017a. Site U1480. In McNeill LC, Dugan B, Petronotis KE, and the  
831 Expedition 362 Scientists, Sumatra Subduction Zone. Proceedings of the  
832 International Ocean Discovery Program, 362: College Station, TX (International  
833 Ocean Discovery Program). <https://doi.org/10.14379/iodp.proc.362.103.2017>

834 McNeill LC, Dugan B, Petronotis KE, Backman J, Bourlange S, Chemale F, Chen W,  
835 Colson TA, Frederik MCG, Guèrin G, Hamahashi M, Henstock T, House BM,  
836 Hüpers, A, Jeppson TN, Kachovich S, Kenigsberg AR, Kuranaga M, Kutterolf S,  
837 Milliken, KL, Mitchison FL, Mukoyoshi H, Nair N, Owari S, Pickering, KT,  
838 Poudoux HFA, Yehua S, Song I, Torres ME, Vannucchi P, Vrolijk PJ, Yang  
839 T, Zhao, X. 2017b. Site U1481. In McNeill LC, Dugan B, Petronotis KE, and  
840 the Expedition 362 Scientists, Sumatra Subduction Zone. Proceedings of the  
841 International Ocean Discovery Program, 362: College Station, TX (International  
842 Ocean Discovery Program). <https://doi.org/10.14379/iodp.proc.362.104.2017>

843 Meiboom S, Gill D. 1958. Modified Spin-Echo Method for Measuring Nuclear  
844 Relaxation Times. Review of Scientific Instruments. 29(8):688–691.  
845 <https://doi.org/10.1063/1.1716296>

846 Misyura, S. 2016. The influence of porosity and structural parameters on different kinds  
847 of gas hydrate dissociation. Science Report 6, 30324.  
848 <https://doi.org/10.1038/srep30324>

849 Moore JC, Vrolijk P. 1992. Fluids in accretionary prisms. Reviews of Geophysics.  
850 30(2):113. <https://doi.org/10.1029/92RG00201>

851 Mountjoy JJ, McKean J, Barnes PM, Pettinga JR. 2009. Terrestrial-style slow-moving  
852 earthflow kinematics in a submarine landslide complex. Marine Geology.  
853 267(3–4):114–127. <https://doi.org/10.1016/j.margeo.2009.09.007>

854 Mountjoy JJ, Barnes PM. 2011. Active upper plate thrust faulting in regions of low  
855 plate interface coupling, repeated slow slip events, and coastal uplift: Example  
856 from the Hikurangi Margin, New Zealand. Geochemistry, Geophysics,  
857 Geosystems. 12(1). <https://doi.org/10.1029/2010GC003326>

858 Mountjoy J, Pecher I, Henrys S, Barnes P, Plaza-Faverola A. 2013. Creeping  
859 deformation mechanisms for mixed hydrate-sediment submarine landslides. In:  
860 EGU General Assembly Conference Abstracts. EGU2013-3489.

861 Mountjoy JJ, Pecher I, Henrys S, Crutchley G, Barnes PM, Plaza-Faverola A. 2014.  
862 Shallow methane hydrate system controls ongoing, downslope sediment  
863 transport in a low-velocity active submarine landslide complex, Hikurangi  
864 Margin, New Zealand. *Geochemistry, Geophysics, Geosystems*. 15(11):4137–  
865 4156. <https://doi.org/10.1002/2014GC005379>

866 Mulder T, Cochonat P. 1996. Classification of offshore mass movements. *Journal*  
867 *of Sedimentary Research* 66, 43–57. <https://doi.org/10.1306/D42682AC-2B26-11D7-8648000102C1865D>

869 Nimblett J, Ruppel C. 2003. Permeability evolution during the formation of gas  
870 hydrates in marine sediments. *Journal of Geophysical Research: Solid Earth*.  
871 108(B8):2420-2003. <https://doi.org/10.1029/2001JB001650>

872 Nishiyama N, Yokoyama T. 2014. Estimation of permeability of sedimentary rocks by  
873 applying water-expulsion porosimetry to Katz and Thompson model.  
874 *Engineering Geology*. 177:75–82. <https://doi.org/10.1016/j.enggeo.2014.05.016>

875 Paull CK, Ussler W, III, 2001. History and significance of gas sampling during DSDP  
876 and ODP drilling associated with gas hydrates. In Paull, C.K., and Dillon, W.P.  
877 (Eds.), *Natural Gas Hydrates: Occurrence, Distribution, and Detection*.  
878 *Geophysical Monograph*, 124:53–66. <https://doi.org/10.1029/GM124p0053>

879 Pecher IA, Mountjoy JJ, Crutchley G, Henrys S, Torres ME, Huhn K, Kukowski N,  
880 Santamarina C, Riedel M, Strasser M, Bialas J, Krastel S, Vanneste M. 2014.  
881 *Creeping Gas Hydrate Slides: Slow Deformation of Submarine Landslides on*  
882 *the Hikurangi Margin*. IODP Original proposal 841-Apl2.

883 Pecher IA, Barnes PM, LeVay LJ, Bourlange SM, Brunet MMY, Cardona S, Clennell  
884 MB, Cook AE, Crundwell MP, Dugan B, Elger J, Gamboa D, Georgiopoulou A,  
885 Greve A, Han S, Heeschen KU, Hu G, Kim GY, Kitajima H, Koge H, Li X,  
886 Machado KS, McNamara DD, Moore GF, Mountjoy JJ, Nole MA, Owari S,  
887 Paganoni M, Petronotis KE, Rose PS, Sreaton EJ, Shankar U, Shepherd CL,  
888 Torres ME, Underwood MB, Wang X, Woodhouse AD, Wu H-Y. 2019.  
889 *Expedition 372A methods*. In: Pecher IA, Barnes PM, LeVay LJ and the  
890 *Expedition 372A Scientists, Creeping Gas Hydrate Slides*. *Proceedings of the*  
891 *International Ocean Discovery Program, 372A: College Station, TX*  
892 *(International Ocean Discovery Program)*.  
893 <https://doi.org/10.14379/iodp.proc.372A.102.2019>

894 Pedley KL, Barnes PM, Pettinga JR, Lewis KB. 2010. Seafloor structural geomorphic  
895 evolution of the accretionary frontal wedge in response to seamount subduction,  
896 Poverty Indentation, New Zealand. *Marine Geology*. 270(1–4):119–138.  
897 <https://doi.org/10.1016/j.margeo.2009.11.006>

898 Purcell WR. 1949. Capillary Pressures - Their Measurement Using Mercury and the  
899 Calculation of Permeability Therefrom. *Journal of Petroleum Technology*.  
900 1(02):39–48. <https://doi.org/10.2118/949039-G>

901 Reuschlé T, 2011. Data report: permeability measurements under confining pressure,  
902 Exp. 315 and 316, Nankai Trough. In: Kinoshita M, Tobin H, Ashi J, Kimura G,  
903 Lallemand S, Screatton EJ, Curewitz D, Masago H, Moe KT and the Expedition  
904 314/315/316 Scientists, *Proceedings of the Integrated Ocean Drilling Program*,  
905 314/315/316: Washington, DC,  
906 <https://doi.org/10.2204/iodp.proc.314315316.205.2011>.

907 Revil A, Cathles LM, Losh S, Nunn JA. 1998. Electrical conductivity in shaly sands  
908 with geophysical applications. *Journal of Geophysical Research: Solid Earth*.  
909 103(B10):23925–23936. <https://doi.org/10.1029/98JB02125>

910 Rosenberger K, Underwood, MB, Vrolijk P, Haines S. 2020. Data report: clay mineral  
911 assemblages in hemipelagic sediments entering the Sumatra subduction zone,  
912 IODP Sites U1480 and U1481, Expedition 362. In McNeill LC, Dugan B,  
913 Petronotis KE, and the Expedition 362 Scientists. *Sumatra Subduction Zone*.  
914 *Proceedings of the International Ocean Discovery Program*, 362: College  
915 Station, TX (International Ocean Discovery Program).  
916 <https://doi.org/10.14379/iodp.proc.362.204.2020>

917 Saffer DM, Wallace LM, Barnes PM, Pecher IA, Petronotis KE, LeVay LJ, Bell RE,  
918 Crundwell MP, Engelmann de Oliveira CH, Fagereng A, Fulton PM, Greve A,  
919 Harris RN, Hashimoto Y, Hüpers A, Ikari MJ, Ito Y, Kitajima H, Kutterolf S,  
920 Lee H, Li X, Luo M, Malie PR, Meneghini F, Morgan JK, Noda A, Rabinowitz  
921 HS, Savage HM, Shepherd CL, Shreedharan S, Solomon EA, Underwood MB,  
922 Wang M, Woodhouse AD, Bourlange SM, Brunet MMY, Cardona S, Clennell  
923 MB, Cook AE, Dugan B, Elger J, Gamboa D, Georgiopoulou A, Han S,  
924 Heeschen KU, Hu G, Kim GY, Koge H, Machado KS, McNamara DD, Moore  
925 GF, Mountjoy JJ, Nole MA, Owari S, Paganoni M, Rose PS, Screatton EJ,

926 Shankar U, Torres ME, Wang X, Wu H-Y. 2019. Expedition 372B/375  
927 summary. <https://doi.org/10.14379/iodp.proc.372B375.101.2019>

928 Screaton E, Saffer D, Henry P, Hunze S. 2002. Porosity loss within the underthrust  
929 sediments of the Nankai accretionary complex: Implications for overpressures.  
930 *Geology*. 30(1):19. [https://doi.org/10.1130/0091-  
931 7613\(2002\)030<0019:PLWTUS>2.0.CO;2](https://doi.org/10.1130/0091-7613(2002)030<0019:PLWTUS>2.0.CO;2)

932 Screaton, E.J., Torres, M.E., Dugan, B., Heeschen, K.U., Mountjoy, J.J., Ayres, C.,  
933 Rose, P.S., Pecher, I.A., Barnes, P.M., and LeVay, L.J. (2019). Sedimentation  
934 Controls on Methane-Hydrate Dynamics Across Glacial/Interglacial Stages: An  
935 Example From International Ocean Discovery Program Site U1517, Hikurangi  
936 Margin. *Geochemistry, Geophysics, Geosystems*. 20 (11):4906-4921.  
937 <https://doi.org/10.1029/2019GC008603>.

938 Screaton EJ, Torres ME, Dugan B, Heeschen KU, Mountjoy JJ, Ayres C, Rose PS,  
939 Pecher IA, Barnes PM, LeVay LJ. 2020. Reply to Comments by N. Sultan on  
940 “Sedimentation Controls on Methane-Hydrate Dynamics Across  
941 Glacial/Interglacial Stages: An Example From International Ocean Discovery  
942 Program Site U1517, Hikurangi Margin.” *Geochemistry, Geophysics,  
943 Geosystems*. 21(6). <https://doi.org/10.1029/2020GC009005>

944 Screaton EJ, Summerfield C, Jaeger JM, Whipple J. 2021. Data report: permeability and  
945 grain size of sediments, IODP Expeditions 372 and 375. In: Wallace LM, Saffer  
946 DM, Barnes PM, Pecher IA, Petronotis KE, LeVay LJ and the Expedition  
947 372/375 Scientists, Hikurangi Subduction Margin Coring and Observatories.  
948 *Proceedings of the International Ocean Discovery Program, 372B/375: College  
949 Station, TX (International Ocean Discovery Program)*  
950 <https://doi.org/10.14379/iodp.proc.372B375.205.2021>

951 Shen P, Li G, Li B, Li X. 2020. Coupling effect of porosity and hydrate saturation on  
952 the permeability of methane hydrate-bearing sediments. *Fuel*. 269. 117425.  
953 <https://doi.org/10.1016/j.fuel.2020.117425>

954 Sultan N. 2020. Comment on “Sedimentation Controls on Methane-Hydrate Dynamics  
955 Across Glacial/Interglacial Stages: An Example From International Ocean  
956 Discovery Program Site U1517, Hikurangi Margin” by E. J. Sreaton et al.  
957 *Geochemistry, Geophysics, Geosystems*. 21(6).  
958 <https://doi.org/10.1029/2019GC008846>

959 Underwood MB, Dugan B, 2021. Data report: clay mineral assemblages within and  
960 beneath the Tuaheni landslide complex, IODP Site U1517, offshore New  
961 Zealand. In Pecher I.A, Barnes PM, LeVay LJ and the Expedition 372A  
962 Scientists, Creeping Gas Hydrate Slides. Proceedings of the International Ocean  
963 Discovery Program, 372A: College Station, TX (International Ocean Discovery  
964 Program). <https://doi.org/10.14379/iodp.proc.372A.201.2021>

965 Underwood MB. 2021. Data report: clay mineral assemblages within trench-floor and  
966 accreted trench-floor deposits, IODP Expedition 372B/375 Sites U1518 and  
967 U1520, offshore New Zealand. In Wallace LM, Saffer DM, Barnes PM, Pecher  
968 IA, Petronotis KE, LeVay LJ and the Expedition 372/375 Scientists, Hikurangi  
969 Subduction Margin Coring, Logging, and Observatories. Proceedings of the  
970 International Ocean Discovery Program, 372B/375: College Station, TX  
971 (International Ocean Discovery Program).  
972 <https://doi.org/10.14379/iodp.proc.372B375.206.2021>

973 Underwood MB, Dugan B. 2021. Data report: clay mineral assemblages within and  
974 beneath the Tuaheni Landslide Complex, IODP Expedition 372A Site U1517,  
975 offshore New Zealand. In Pecher, I.A., Barnes, P.M., LeVay, L.J., and the  
976 Expedition 372A Scientists, Creeping Gas Hydrate Slides. Proceedings of the  
977 International Ocean Discovery Program, 372A: College Station, TX  
978 (International Ocean Discovery Program).  
979 <https://doi.org/10.14379/iodp.proc.372A.201.2021>

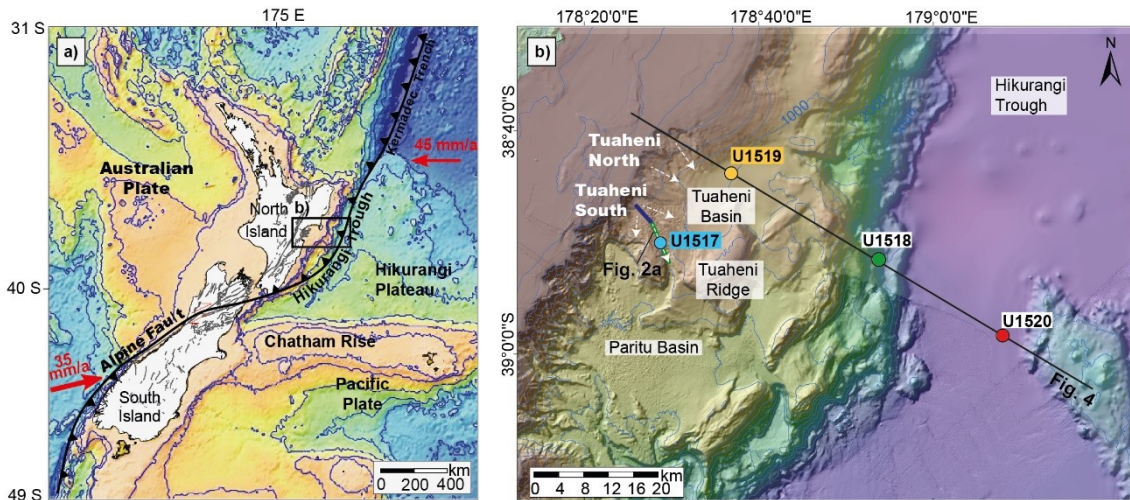
980 Waite WF et al. 2009. Physical properties of hydrate-bearing sediments, Reviews of  
981 Geophysics. 47, RG4003, <https://doi.org/10.1029/2008RG000279>.

982 Wallace LM, Beavan J, McCaffrey R, Desmond D. 2004. Subduction zone coupling and  
983 tectonic block rotations in the North Island, New Zealand. Journal of  
984 Geophysical Research. 109(B12). <https://doi.org/10.1029/2004JB003241>

985 Wallace LM, Saffer DM, Barnes PM, Pecher IA, Petronotis KE, LeVay LJ, Bell RE,  
986 Crundwell MP, Engelmann de Oliveira CH, Fagereng A, Fulton PM, Greve A,  
987 Harris RN, Hashimoto Y, Hüpers A, Ikari MJ, Ito Y, Kitajima H, Kutterolf S,  
988 Lee H, Li X, Luo M, Malie PR, Meneghini F, Morgan JK, Noda A, Rabinowitz  
989 HS, Savage HM, Shepherd CL, Shreedharan S, Solomon EA, Underwood MB,  
990 Wang M, Woodhouse AD, Bourlange SM, Brunet MMY, Cardona S, Clennell  
991 MB, Cook AE, Dugan B, Elger J, Gamboa D, Georgiopoulou A, Han S,

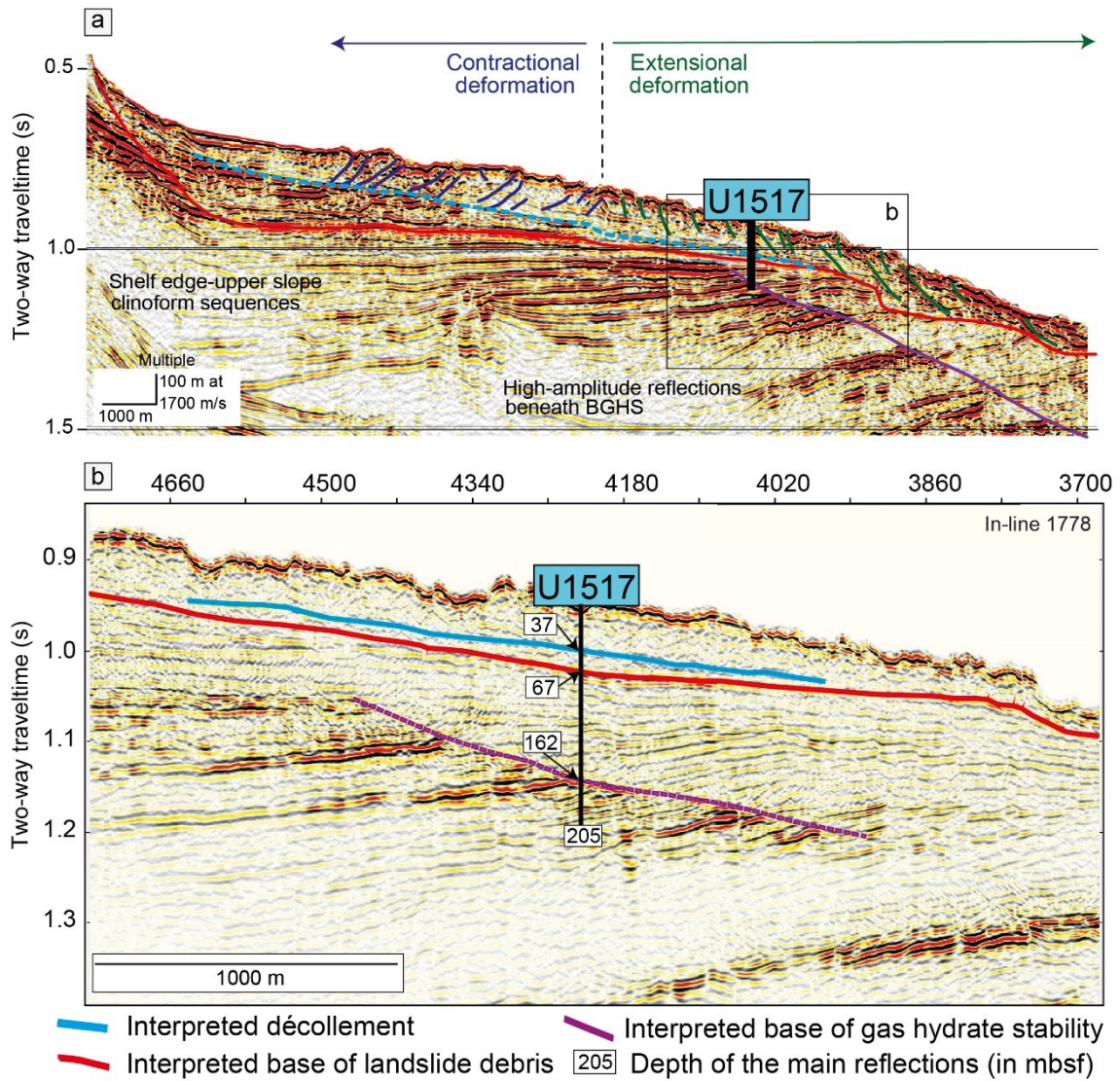
992 Heeschen KU, Hu G, Kim GY, Koge H, Machado KS, McNamara DD, Moore  
993 GF, Mountjoy JJ, Nole MA, Owari S, Paganoni M, Rose PS, Screatton EJ,  
994 Shankar U, Torres ME, Wang X, Wu, H-Y. 2019. Expedition 372B/375  
995 methods, <https://doi.org/10.14379/iodp.proc.372B375.102.2019>  
996 Walsh JB. 1981. Effect of pore pressure and confining pressure on fracture  
997 permeability. International Journal of Rock Mechanics and Mining Sciences &  
998 Geomechanics Abstracts, 18:429-435, [https://doi.org/10.1016/0148-  
999 9062\(81\)90006-1](https://doi.org/10.1016/0148-9062(81)90006-1).  
1000 Wang L, Gu LJ, Lu HL. 2020. Sediment permeability change on natural gas hydrate  
1001 dissociation induced by depressurization. China Geology 3(2):221-229.  
1002 <https://doi.org/10.31035/cg2020039>  
1003 Wei J, Wu T, Feng X, Liang J, Li W, Xie R, Wu G. 2021. Physical Properties of Gas  
1004 Hydrate-Bearing Pressure Core Sediments in the South China Sea. Geofluids.  
1005 <https://doi.org/10.1155/2021/6636125>  
1006

1007 **Figures**



1008  
 1009 Figure 1. a) Tectonic setting of the Hikurangi margin with plate motion indicated by red  
 1010 arrows (modified after Barnes et al., 2019a). b) Bathymetric map of the IODP  
 1011 Expeditions 372/375 study area offshore Gisborne located on a) (modified after  
 1012 Mountjoy et al., 2014 and Saffer et al., 2019). The thick line represents the seismic  
 1013 profile TAN1114-10b shown in Figure 2a with the location of Site U1517. The blue  
 1014 (respectively, green) section of this line indicates the contractional (respectively,  
 1015 extensional) zone of the slide represented in Figure 2a. The black line represents the  
 1016 seismic profile 05CM-04 across the margin with the location of Site U1519 and of other  
 1017 Sites from IODP Expeditions 372-375. White dashed arrows display the direction of  
 1018 movement within the landslides of the North and South Tuaheni (after Mountjoy et al.,  
 1019 2014).





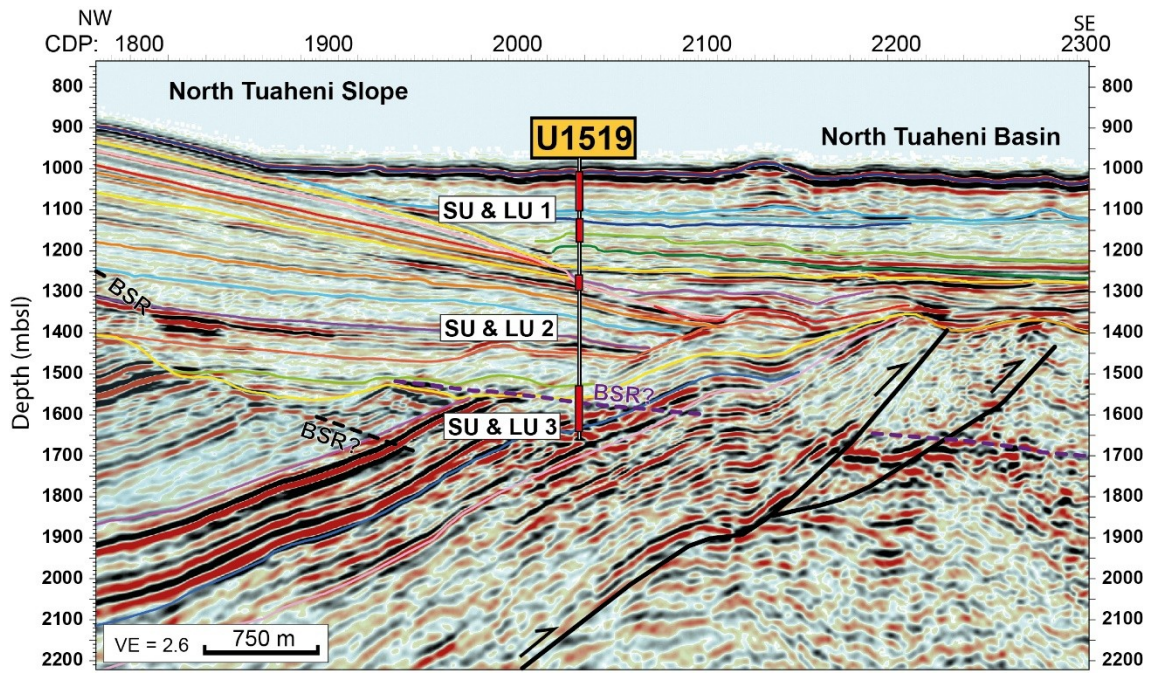
1020

1021 Figure 2. a) Seismic profile TAN1114-10b across the South Tuaheni landslide  
 1022 (modified after Mountjoy et al., 2014 and Barnes et al., 2019a) with b) a zoom in on  
 1023 Site U1517 in the extensional part and the main seismic reflectors (in-line 1778), with  
 1024 the depth in metres below sea floor (modified after Barnes et al., 2019a). BGHS: base of  
 1025 the gas hydrate stability zone.

1026

1027

1028



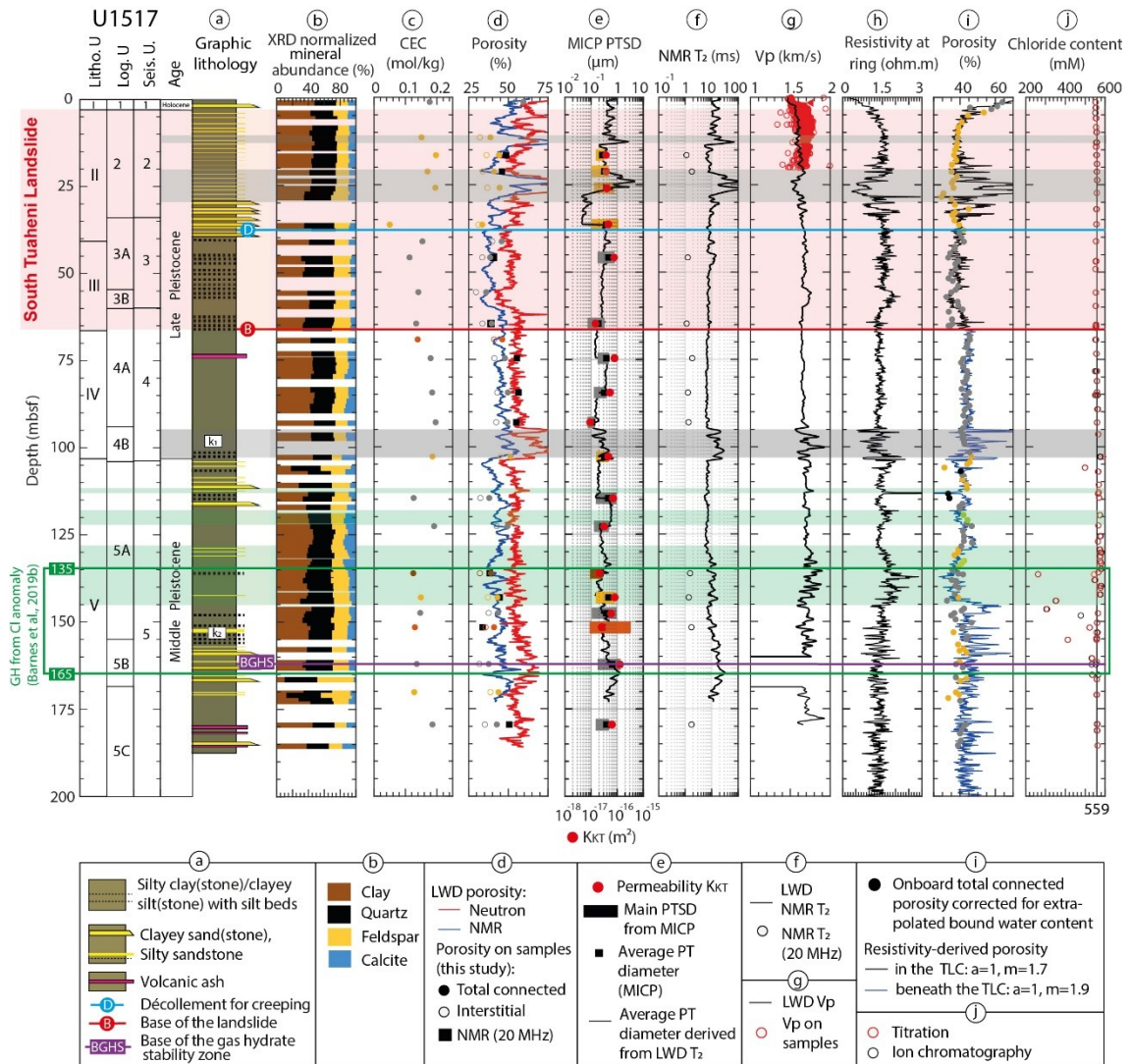
1029

1030 Figure 3. Zoom in on seismic profile 05CM-04 (Figure 1b) on Site U1519 showing the

1031 cored sections (red bars), logging units (LU) and seismic units (SU) (modified after

1032 Barnes et al., 2019c). VE: vertical exaggeration; BSR: bottom-simulating-reflector.

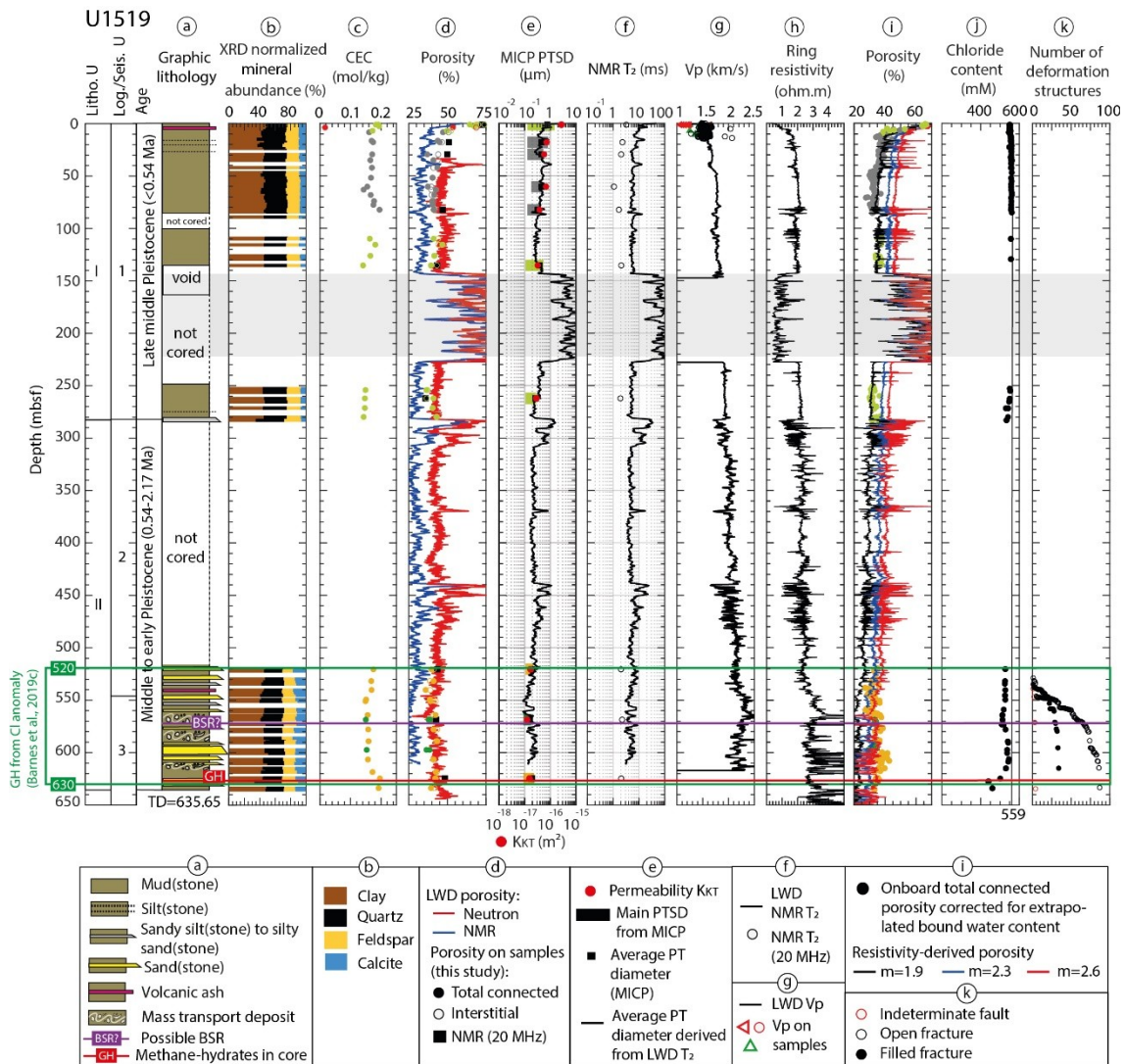
1033



1034

1035 Figure 4. Summary of lithological, logging and seismic units and description (a),  
 1036 mineralogical (b), chemical (c and j) and physical (d, e, f, g, h, i) properties at Site  
 1037 U1517. For (c), (d), (e) and (i), the colour of data points or bars indicates the lithology  
 1038 of the samples analysed: light green for clay(stone); black for silt(stone); gold for  
 1039 alternating sand(stone) and mud(stone) layers; grey for silty clay(stone), clayey  
 1040 silt(stone) or alternating silt and clay layers; orange for clayey silt(stone) with sand;  
 1041 brown for silt(stone) with sand.  $k_1$  and  $k_2$  indicate the location of cores 17H6 and 29F3  
 1042 respectively for permeability measurements. XRD: X-Ray diffraction; CEC: Cation  
 1043 exchange capacity; Kkt: Katz–Thompson permeability; MICP PT(SD): mercury  
 1044 injection capillary pressure pore throat (size distribution) determined based on Bertrand

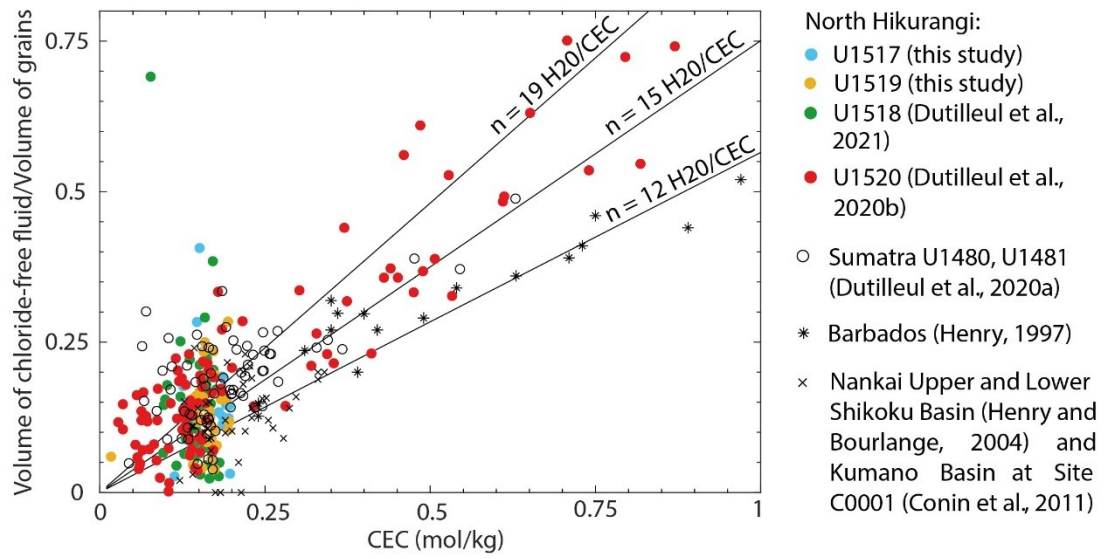
1045 et al. (2021); NMR: nuclear magnetic resonance;  $T_2$ : transverse relaxation time; LWD:  
1046 logging-while-drilling;  $V_p$ : P-wave velocity; TLC: Tuaheni Landslide Complex. The  
1047 red shaded zone represents the landslide mass with marker horizons D and B. The three  
1048 green shaded zones highlight zones expected to host gas hydrates based on LWD data.  
1049 The green rectangle indicates the zone hosting gas hydrates from chloride anomalies  
1050 (Barnes et al., 2019b). In j), 559 mM is the average chloride concentration in modern  
1051 seawater. The base of the gas hydrate stability zone (BGHS) is located at 162 mbsf  
1052 (Screaton et al., 2019). The grey shaded zones are interpreted onboard as washout zones  
1053 between ~10-13 mbsf, ~21-28 mbsf and ~94-104 mbsf (Barnes et al., 2019a).  
1054



1055

1056 Figure 5. Summary of lithological, logging and seismic units and description (a),  
 1057 mineralogical (b), chemical (c and j), physical (d, e, f, g, h, i) and structural (k)  
 1058 properties at Site U1519. For (c), (d), (e) and (i), the colour of data points or bars  
 1059 indicates the lithology of the samples analysed: light green for clay(stone); green for  
 1060 contorted mud(stone); grey for silty clay(stone); red for ash. XRD: X-Ray diffraction;  
 1061 CEC: cation exchange capacity; Kkt: Katz–Thompson permeability; MICP PT(SD):  
 1062 mercury injection capillary pressure pore throat (size distribution) determined based on  
 1063 Bertrand et al. (2021); NMR: nuclear magnetic resonance; T<sub>2</sub>: transverse relaxation  
 1064 time; LWD: logging-while-drilling; Vp: P-wave velocity. The green rectangle  
 1065 highlights a zone of gas hydrate occurrence inferred from chloride data. The grey

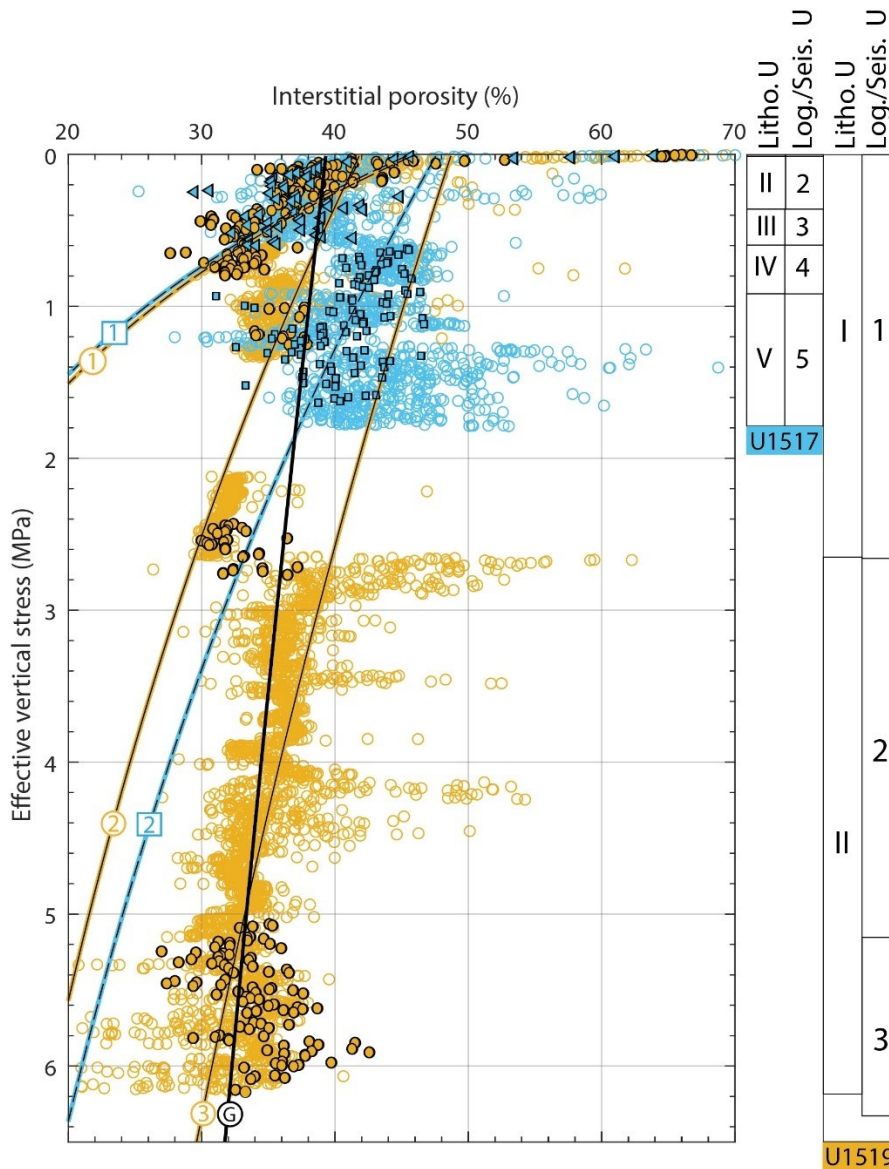
1066 shaded zone represents a washout interval ~143-227 mbsf identified onboard (Barnes et  
1067 al., 2019c). In i), the average chloride concentration in modern seawater is 559 mM. A  
1068 possible bottom-simulating-reflector (BSR) is located at 560 mbsf.  
1069



1070

1071 Figure 6. Bound water ratio versus Cation Exchange Capacity (CEC) at north Hikurangi  
 1072 margin including Site U1517 and U1519, Site U1520 (reference site across the  
 1073 undeformed entering sedimentary section) and U1518 (active thrust at the deformation  
 1074 front) and at other subduction zones from previous works.

1075



Core data: Onboard total connected porosity corrected from extrapolated bound water content at:

Site U1517:

▲ Lithological Units I-III, across the TLC

■ Lithological Units IV & V, below the TLC

● Site U1519

Resistivity-derived porosity (washout intervals excluded):

○ Site U1517

○ Site U1519

Compaction trends:

— from resistivity-derived porosity

- - from core data

U1517:

①  $\Phi_i = 45.6 \exp(-0.57\sigma_v')$ ;  $R^2 = 0.40$

②  $\Phi_i = 47.6 \exp(-0.14\sigma_v')$ ;  $R^2 = 0.23$

U1519:

①  $\Phi_i = 46.1 \exp(-0.55\sigma_v')$ ;  $R^2 = 0.45$

②  $\Phi_i = 41.88 \exp(-0.13\sigma_v')$ ;  $R^2 = 0.37$

③  $\Phi_i = 48.7 \exp(-0.08\sigma_v')$ ;  $R^2 = 0.34$

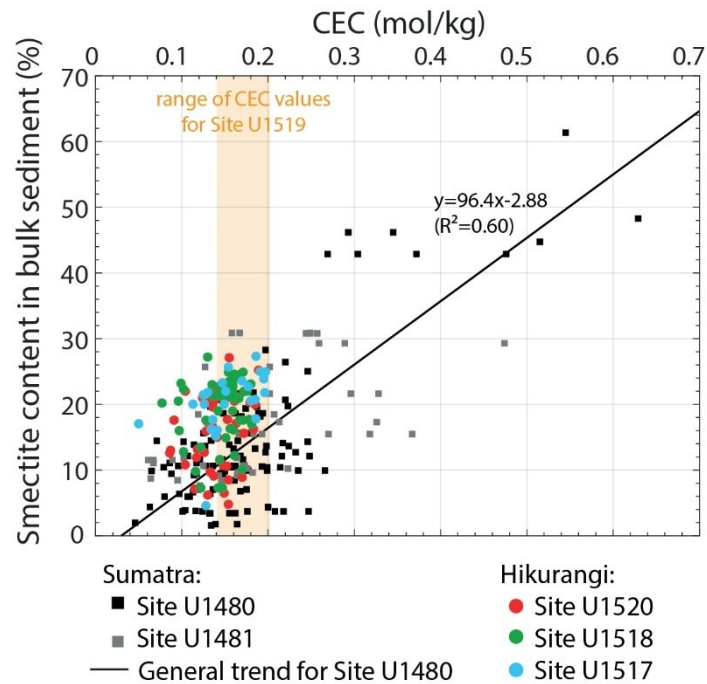
ⓐ  $\Phi_i = 39.3 \exp(-0.03\sigma_v')$ ;  $R^2 = 0.16$

1076

1077 Figure 7. Summary of ring resistivity-derived porosity (open circles) calibrated to  
 1078 onboard interstitial porosity (i.e. total connected porosity corrected for extrapolated  
 1079 bound water content) (triangles, squares or circles) and compaction curves at Site  
 1080 U1517 (light blue) and U1519 (gold). Compaction curves determined from resistivity-



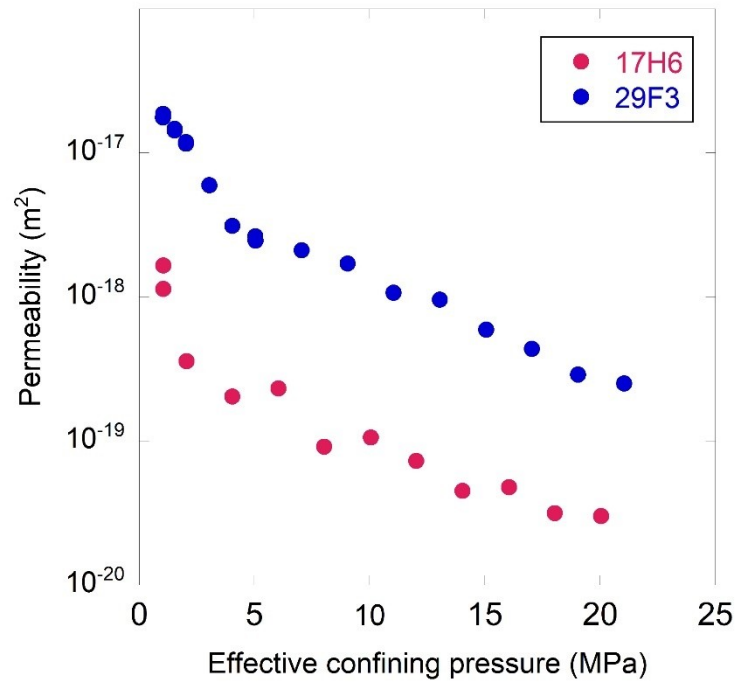
1081 derived porosity and ‘onboard interstitial porosity’ are shown with solid lines and  
1082 dashed lines respectively. The general compaction curve (trend G) at Site U1519  
1083 (excluding the washout interval ~148-227 mbsf) determined from resistivity-derived  
1084 porosity is  $\phi_i = 39.3 e^{-0.03\sigma_v}$  ( $R^2=0.16$ ). At Site U1519, distinct compaction trends are  
1085 given (gold line numbered in open circles): trend 1) for clayey siltstones/silty claystones  
1086 in lithological Unit I, trend 2) for mudstones of the same unit and trend 3) for Unit II. At  
1087 Site U1517 (blue line numbered in open squares), two compaction trends were  
1088 determined from onboard interstitial porosity: trend 1) is the trend for the South TLC  
1089 interval and trend 2) is valid for the preslide interval.  
1090



1091

1092 Figure 8. Relation between smectite content in bulk sediment determined by X-ray  
 1093 diffraction and cation exchange capacity (CEC) values at different IODP Sites in north  
 1094 Sumatra margin and north Hikurangi margin. Smectite content in bulk sediments and  
 1095 CEC are measured on near-by but different samples. Smectite content in bulk sediments  
 1096 for Sumatra Sites U1480 and U1481 are calculated from the XRD analysis of the clay  
 1097 fraction of Rosenberger et al. (2020) and the total clay mineral content of the nearest  
 1098 sample given in McNeill et al. (2017a and b). Smectite content in bulk sediments for  
 1099 Hikurangi Sites U1520 and U1518 are from Underwood (2021) and are from  
 1100 Underwood and Dugan (2021) and S. Cardona (pers. comm.) for Site U1517. CEC data  
 1101 for Sumatra Sites are from Dutilleul et al. (2020a). CEC data for Hikurangi Sites U1520  
 1102 and U1518 are from Dutilleul et al. (2020b) and (in press) respectively.

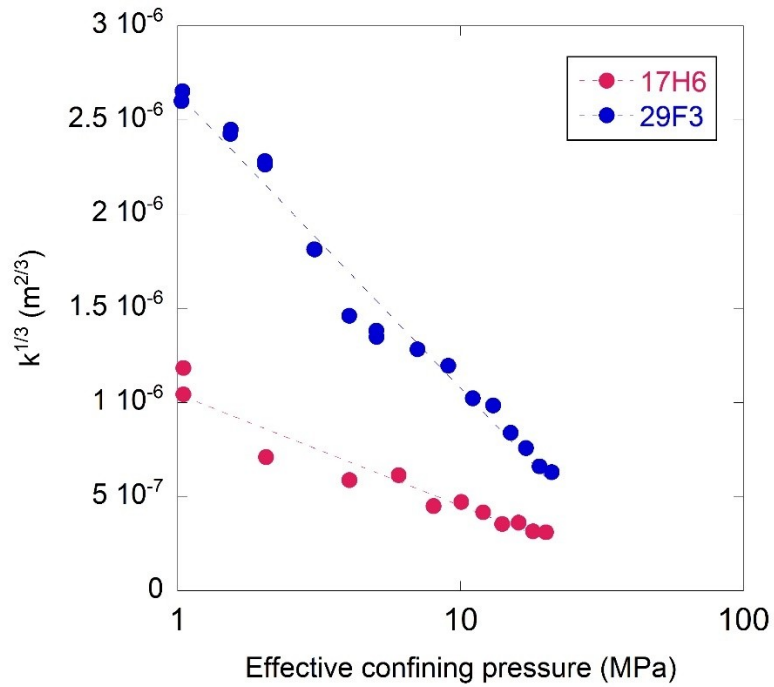
1103



1104

1105 Figure 9. Permeability  $k$  as a function of effective confining pressure  $P_{\text{eff}}$  at in situ pore  
 1106 pressure conditions for samples 17H6 (97.43 mbsf; clayey silt) and 29F3 (157.83 mbsf;  
 1107 alternating sand and mud layers) from Site U1517.

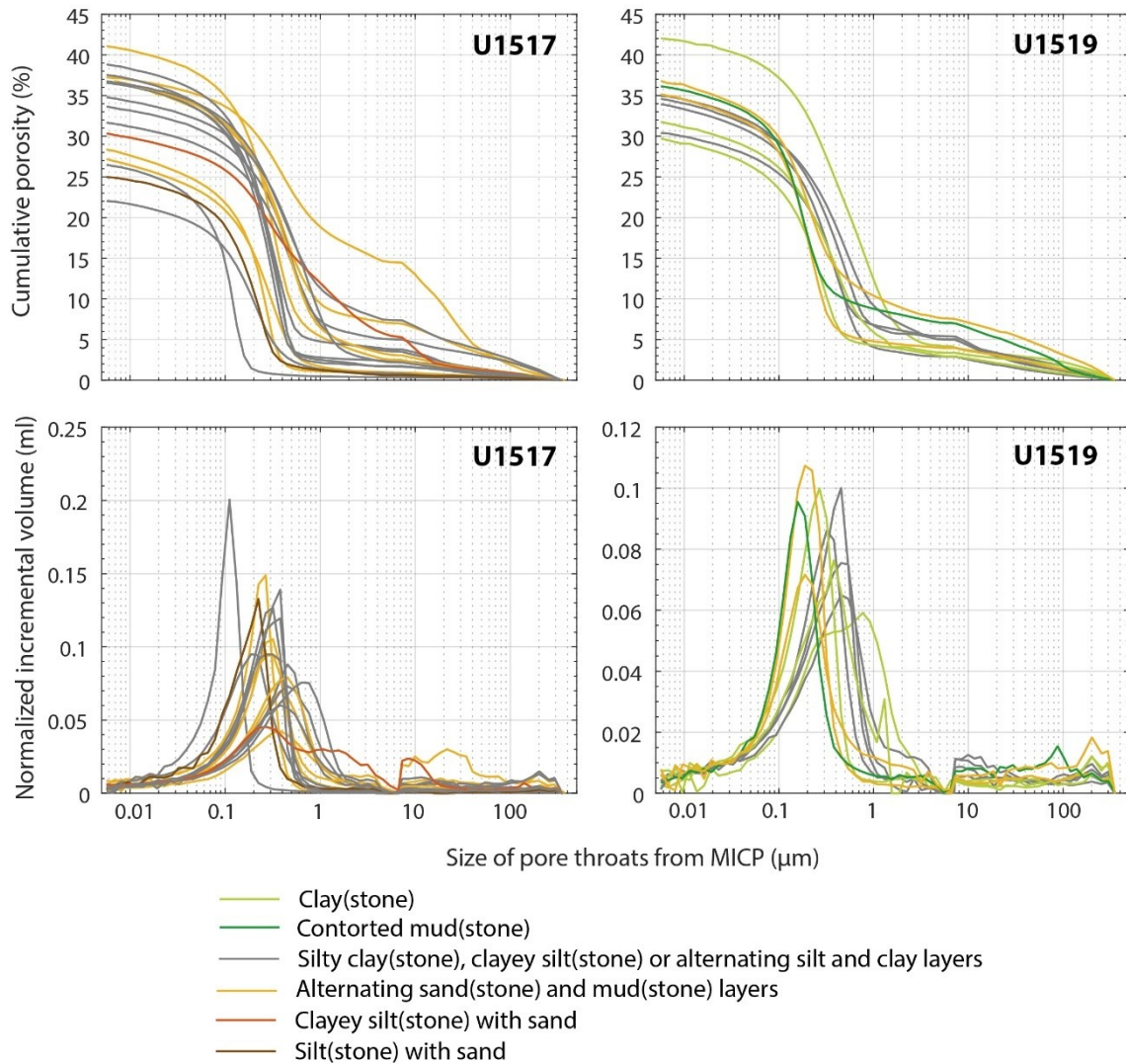
1108



1109

1110 Figure 10. Permeability data of Figure 9 plotted as  $k^{1/3}$  as a function of  $P_{eff}$  in a linear-log  
 1111 graph showing a linear trend consistent with the fracture closure model proposed by  
 1112 Walsh (1981) for samples 17H6 (97.43 mbsf; clayey silt) and 29F3 (157.83 mbsf;  
 1113 alternating sand and mud layers) from Site U1517.

1114



1115

1116 Figure 11. MICP pore-throat size distribution spanning common lithologies at Site

1117 U1517 and U1519 versus cumulative porosity and normalised incremental injection

1118 volume.